A METHODOLOGICAL EVALUATION OF THE ENERGIES IN
DEGRADED ELECTRON BEAMS

A Thesis

Submitted to the Graduate Faculty of the
Louisiana State University and
Agricultural and Mechanical College
in partial fulfillment of the
requirements for the degree of
Master of Science

in

Nuclear Science
(Medical Radiation Science Option)

by
Carrie Ann White
B.S., Nicholls State University, 1980
December 1983

Dedicated to

My Parents,

Florence and Walter White

## TABLE OF CONTENTS

# LIST OF TABLES

## LIST OF FIGURES

# LIST OF FIGURES
## (Continued)

Page

## ABSTRACT

Changes in the geometry of an electron beam can have a profound effect on the energy of the beam. This phenomenon allows a 6 MeV electron beam to be degraded to an energy suitable for the total-skin irradiation technique employed in the treatment of mycosis fungoides. The changes made in the geometry of the 6 MeV beam include the removal of the cone, the extension of the source-surface distance, the interposition of a polystyrene degrader in the beam and the direction of the central axis of the beam oblique to the treatment surface. The effect on the energy of the beam resulting from each change in geometry was determined by measuring the relative ionization curve associated with each different geometry. The ionization curves were compared to determine which geometry change produced the most dramatic reduction in the energy of the beam. The average incident energy and the most probable incident energy were determined for each electron beam according to guidelines set forth in current protocols.

## INTRODUCTION

The principal parameter of an electron beam that makes
it a valuable radiotherapeutic tool is its rapid diminution
of dose with depth.   This special characteristic of the
electron dose distribution allows for the protection of
dose-limiting structures that lie deep to a treatment
volume.   This is in sharp contrast to the exponential ab-
sorption of superficial x-rays which permits a significantly
larger dose to be delivered to underlying tissues (Fig. 1).

Electron beams are considered to be indispensible in
many clinical situations (Tapley 1976).   Beams in the energy
range of 3-10 MeV are most often employed in the irradiation
of skin tumors, lesions near the body surface, the chest
wall, and the total body surface.

One of the more complex applications of low energy
electron beams is in the treatment of mycosis fungoides.
This cutaneous lymphoma which can involve the entire body
surface, is extremely radiosensitive.   Therefore the limited
penetration of the electron beam provides an excellent means
of treating the entire skin surface while providing protec-
tion to the deeper tissues.   In addition, the dose from
scattered radiation to sensitive areas, such as the lens of
the eye, can be readily controlled.
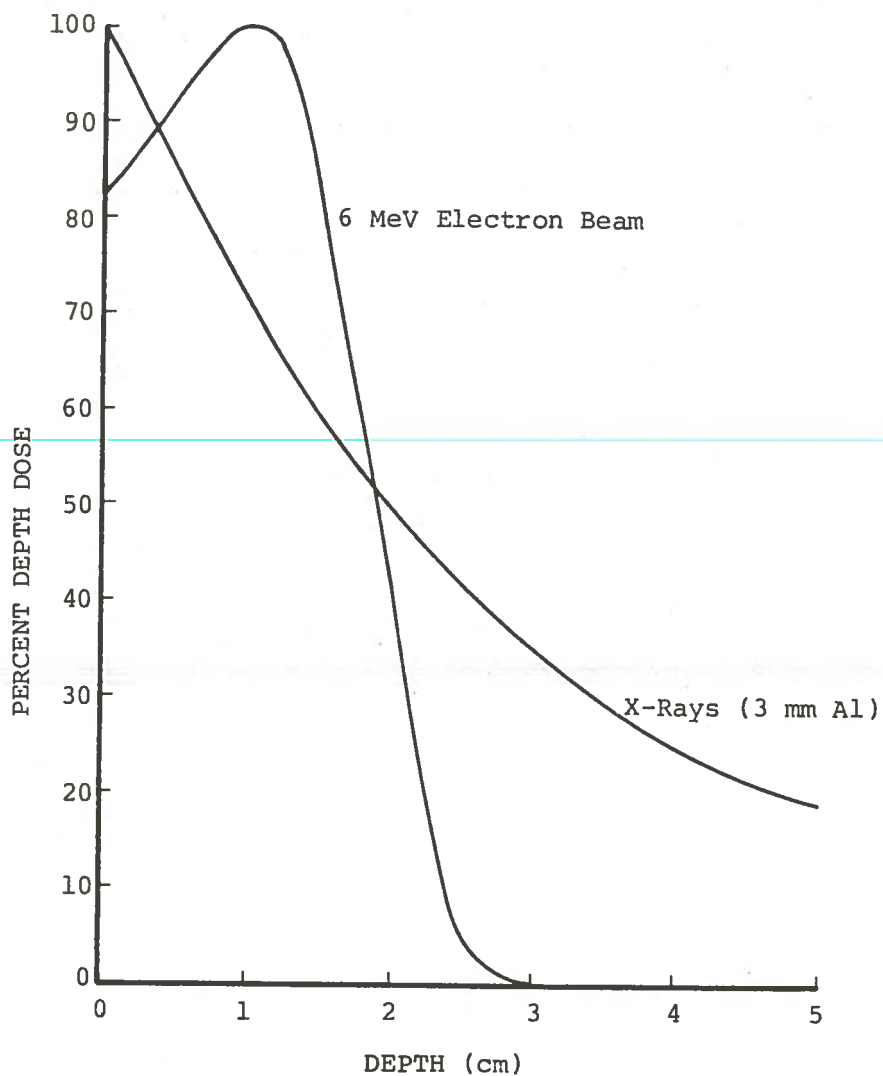
Fig. 1.  Comparison of percent depth dose curves for a 6 MeV electron beam and low energy x-rays.  It is noted that at a depth of 3 cm the dose delivered by the electron beam is essentially zero, while the dose delivered by the superficial x-rays is approximately 37% of the total dose.

Various techniques for total skin electron beam irradiation have been reported (Trump et al. 1943, Karzmark et al. 1960, Page et al. 1970, Nisce et al. 1973). Treatment techniques have varied from one institution to another depending on the equipment available. Common to most techniques, however, is the use of an electron beam in the range of 2-4 MeV.

Patients at the Stanford University School of Medicine have been treated with 4 MeV electrons produced by a Varian Clinac-10 linear accelerator (Hoppe 1979). With the Stanford treatment technique, the patient stands at a distance of 3 meters from the accelerator and the entire exposed surface of the patient is irradiated with a broad dual-exposure field. A field directed horizontally toward the patient does not provide adequate dose uniformity in the vertical plane of the patient. To achieve adequate dose uniformity the beam is directed alternately $20^{\circ}$ above and $20^{\circ}$ below the horizontal plane. Such a $\pm20^{\circ}$ dual-exposure field provides a uniform dose distribution ($\pm4\%$) over an area of approximately 7 X 4 feet (Karzmark et al. 1960). In addition to providing dose uniformity, the $\pm20^{\circ}$ dual-exposure field also directs the central axis of the beam, containing most of the photon contamination, above the patient's head and below the patient's feet. The patient is treated in the standing position with a multiple field technique employing overlapping fields. This technique,

consisting of six fields (anterior, posterior, and four oblique fields) is arranged in 60$^{\circ}$ increments about the vertical axis of the patient. Each treatment, therefore, consists of twelve exposures--six with the gantry directed 20$^{\circ}$ upward and six with the gantry directed 20$^{\circ}$ downward.

In light of the results achieved at Stanford with this technique (Hoppe 1979), the staff at the Perkins Radiation Treatment Center in Baton Rouge, Louisiana have chosen to adopt this technique for the treatment of mycosis fungoides. It was necessary, however, to make a few modifications in the technique due to the available equipment.

Perkins Radiation Center is equipped with a Varian Clinac-18 linear accelerator capable of producing 10 MeV x-rays and 6, 9, 12, 15, and 18 MeV electron beams. Since 6 MeV is the lowest electron energy available, it is necessary to degrade the 6 MeV beam to an energy more appropriate to the treatment (such as 4 MeV). This is accomplished by placing a polystyrene panel, 6 mm thick, between the patient and the source. The patient stands on a platform 3.3 meters from the source of the electron beam. Attached to this platform, 0.33 meter from the patient is the polystyrene panel (degrader).

Although the geometry of the beam employed at Perkins Radiation Center is different from that used at Stanford, the $\pm$20$^{\circ}$ dual-exposure field is applied in the same manner. Film dosimetry studies performed at Perkins Radiation Center

demonstrate that the degree of dose uniformity is consistent with that of Stanford.

Use of this specialized treatment technique requires that the 6 MeV electron beam be used in a manner which is an extreme departure from the normal treatment technique used in most clinical situations. A normal treatment geometry includes an electron beam applicator and a cone which extends to within 5-10 cm of the patient's skin. The source-surface distance (SSD) is usually 1 meter and generally the beam is perpendicular to the treated surface of the patient.

This specialized technique, however, requires that the electron beam applicator and the cone be removed. The collimators are open to full field and the patient is positioned at 3.3 meters, rather than at 1 meter. A degrader is interposed in the beam and, above all, the beam is directed above and below the patient. Each of these changes in geometry has a profound effect on the energy of the beam.

The intent of this study was to determine the effect that these changes have on the energy of the electron beam. Each modification in geometry was studied individually and in a methodological fashion by observing the change produced on the depth ionization curve. The energy of the degraded beam was determined according to guidelines set forth by the International Commission on Radiation Units and Measurements, the Hospital Physicists' Association, and the Nordic Association of Clinical Physics.

# LITERATURE REVIEW

There are several methods of energy measurements that can be used to characterize the energy of an electron beam (Almond 1981a).  Because some of the methods require equipment that is not readily available to the clinical physicist, an indirect method of energy determination is often employed using well established empirical relations (ICRU 1971).

Markus (1961) published a linear equation which expresses a relationship between the energy at the surface of a phantom and the practical range of fast electrons in water:

$$R_p \rho = 0.521 \ E_0 - 0.376$$

where $E_0$ is the energy in MeV, $\rho$ is the density of water, and $R_p$ represents the practical range in centimeters (Fig. 2).  A similar equation which relates the energy at the surface of the phantom to the practical range,

$$R_p = 0.52 \ E_0 - 0.3$$

was recommended by AAPM (1966), Svensson and Hettinger (1970) and NACP (1972).

Precise measurements of the practical range of electrons in water have shown that the energy-range relation of Markus is not truly linear (Nüsse 1969).  However, ICRU
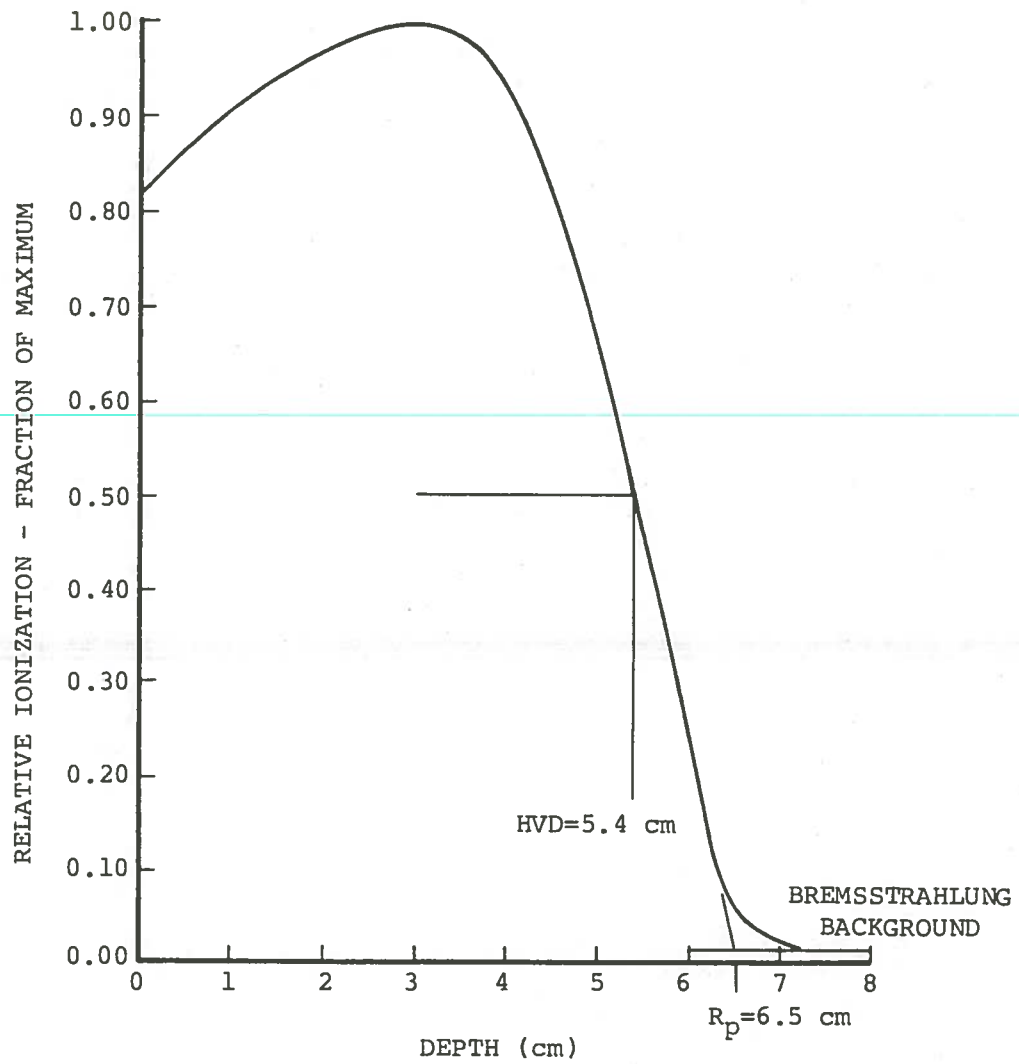
Fig. 2. Relative ionization curve for an electron beam. The practical range, $R_p$, is determined by extrapolating the decreasing portion of the curve down to the bremsstrahlung background. The depth at the point of intersection is the practical range. The half-value depth, HVD, is demonstrated.

(1971) recommends the Markus equation for the determination of the energy at the phantom surface and states that the deviation of the empirical relations from the actual values is less that 2% for electrons from about 5 MeV to 50 MeV.

ICRU (1971) also points out that when the range-energy equation is applied with absorbers in place, such as the window or scattering foils, the energy calculated will be close to the most probable energy, $E_{p,0}$, at the surface. Nüsse (1969) suggests that there are several factors, which influence range measurements. These include geometrical factors, which take into account beam divergence and the influence of beam and detector diameter. Also included are factors which influence particle energy. These take into account energy loss in the accelerator window and energy loss in the air.

Schultz (1969) suggests that the specification of electron beam energy be made by the use of the half value depth (HVD) in water. In a protocol for electrons with energies below 5 MeV, HPA (1975) recommends the use of the HVD and suggests the equation

$$E_0 (\text{MeV}) = 2.5 \text{ MeV cm}^{-1} (\text{HVD})$$

where HVD is the half-value depth (Fig. 2) in polystyrene. A more exact equation for electrons 5 MeV and below is given by Morris and Owen (1975):

$$E_0 = 2.37 \text{ HVD} + 0.19$$

where HVD is the half-value depth in centimeters of poly-styrene. These authors state that since the collision mass stopping power of water is about 3% higher than that of polystyrene, the depths in water and polystyrene are in the ratio of 0.97 to 1. Therefore the correction factor 1.031 can be used to convert from depth in water to depth in poly-styrene.

Morris and Owen (1975) and HPA (1975) fail to specify whether the incident energy, $E_0$, is the average incident energy, $\overline{E}_0$, or the most probable incident energy, $E_{p,0}$. Brahme and Svensson (1976) point out, however, that since the half-value depth is in the region reached by approxi-mately half of the primary electrons, it is likely to be more closely related to the average energy, $\overline{E}_0$, than to the most probable energy, $E_{p,0}$. This theory accounts for the poor agreement found by de Almeida and Almond (1973) between energies determined by the range-energy relationship and the half-value depth relationship.

A protocol published by NACP (1981) for electron beams with mean energies at the phantom surface below 15 MeV recommends NACP (1980) for a full description of the methods to be used for energy determination. According to NACP (1980), the most probable energy at the phantom surface should be determined by the empirical relation

$$E_{p,0} = C_1 + C_2 R_p + C_3 R_p^{\,2}$$

where

$$C_1 = 0.22 \text{ MeV}, \ C_2 = 1.98 \text{ MeV cm}^{-1} \text{ and}$$
$$C_3 = 0.0025 \text{ MeV cm}^{-2}.$$

For the energy range 1 to 50 MeV this relation fits experimental and calculated data to within 2 percent.

This same protocol recommends that the average energy at the surface of the phantom should be determined by relating it to the half value depth. This linear relationship is given by

$$\bar{E}_0 = C_4 HVD$$

where $C_4 = 2.33 \text{ MeV cm}^{-1}$. This equation is also suggested by Brahme and Svensson (1976). NACP (1980) states that this equation should be used in the energy range of 5 to 30 MeV. For energies above and below this range, NACP (1980) supplies a graph and a table which afford a means of determining the energy from the half-value depth.

The most probable energy, $E_{p,0}$, and the average energy, $\bar{E}_0$, are valuable for different reasons. Knowledge of the most probable energy at the phantom surface is important because standardized depth dose curves are sometimes used for accelerators similar to each other in construction and most standardized curves have been correlated to $E_{p,0}$ (Brahme and Svensson 1976). The average energy at the phantom surface is an important parameter in that it is related to the stopping power and the conversion factors which are necessary for dosimetric calculations.

# MATERIALS AND METHODS

## Experimental Design

To evaluate the effects of modifying the geometry of a 6 MeV electron beam*, relative ionization curves were determined for several different beam geometries. The geometries having a source-to-surface distance (SSD) of 100 cm were as follows:

1) 10 X 10 cm cone, 15 x 15 cm collimators (Fig. 3)

2) Cone absent, 15 x 15 cm collimators (Fig. 4)

3) Cone absent, 36 x 36 cm collimators (Fig. 5)

4) Cone absent, 36 x 36 cm collimators, 6 mm thick polystyrene sheet attached to the collimator face (Fig. 6)

The geometries having a source-to-surface distance (SSD) of 333 cm were as follows:

5) Cone absent, 36 x 36 cm collimators (Fig. 7)

6) Cone absent, 36 x 36 cm collimators, 6 mm thick polystyrene sheet attached to the collimator face (Fig. 8)

7) Cone absent, 36 x 36 cm collimators, 6 mm thick polystyrene panel (219 cm x 39 cm) positioned 33 cm in front of the phantom (Fig. 9)

* 6 MeV refers to the nominal energy indicated on the console of the machine. It does not necessarily reflect the accelerator energy.
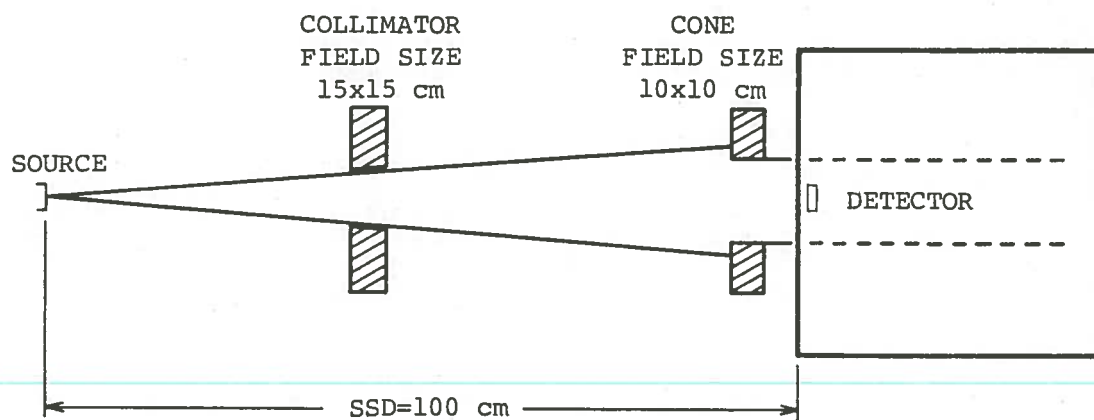
Fig. 3. Diagram of standard 10x10 cm geometry. Beam is directed horizontally toward phantom. Source-surface distance equals 100cm. Cone is in normal treatment position.
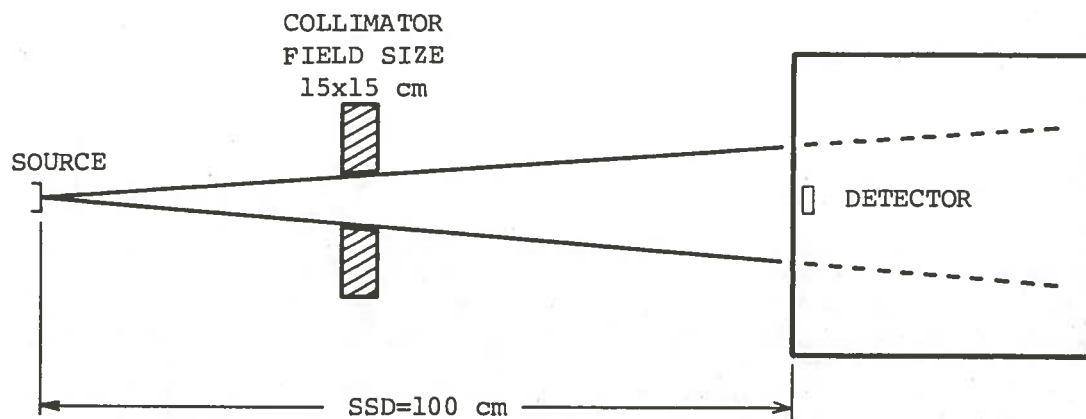


Fig. 4. Diagram of modified geometry. Change in geometry is made by removing the 10x10 cm cone
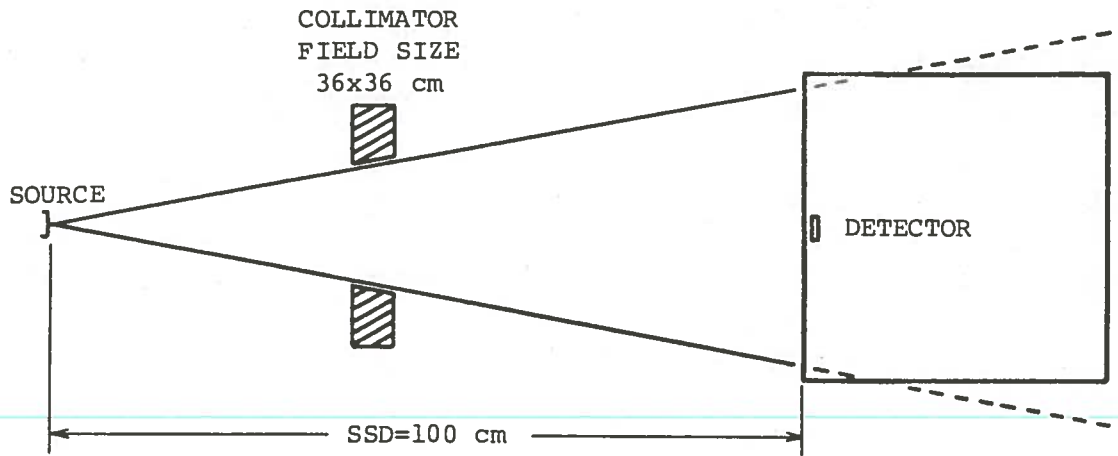
Fig. 5.  Diagram of modified geometry.  Change in geometry is made by opening collimators to 36x36 cm.
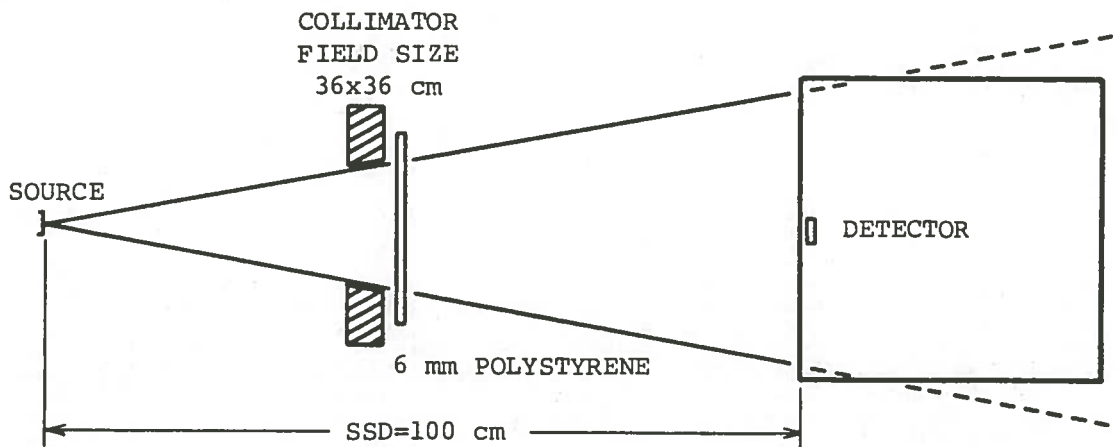


Fig. 6.  Diagram of modified geometry.  A polystyrene sheet 6 mm thick is interposed in the beam by attaching it to the collimator face.
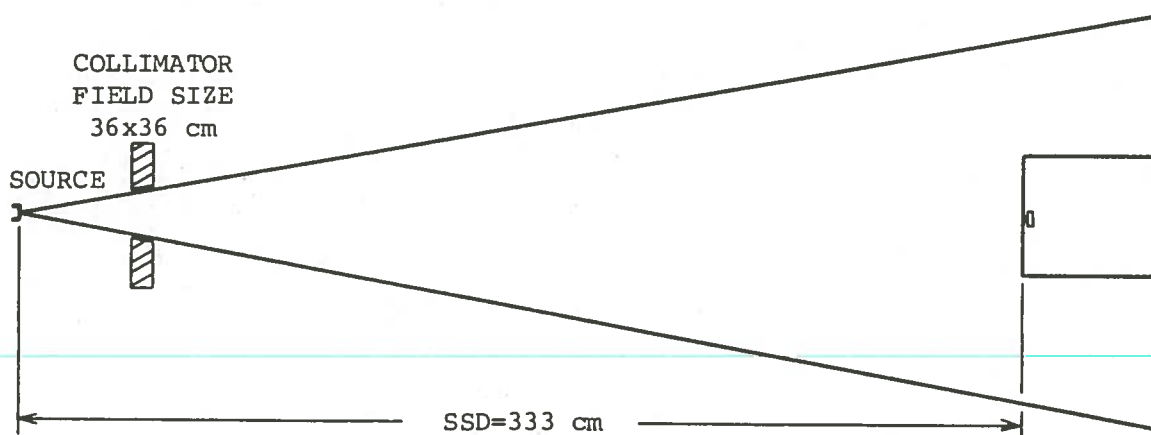
Fig. 7.  Diagram of modified geometry.  Phantom is moved out to a source-surface distance of 333 cm.  The beam is directed horizontally toward the phantom with an open 36x36 cm field.
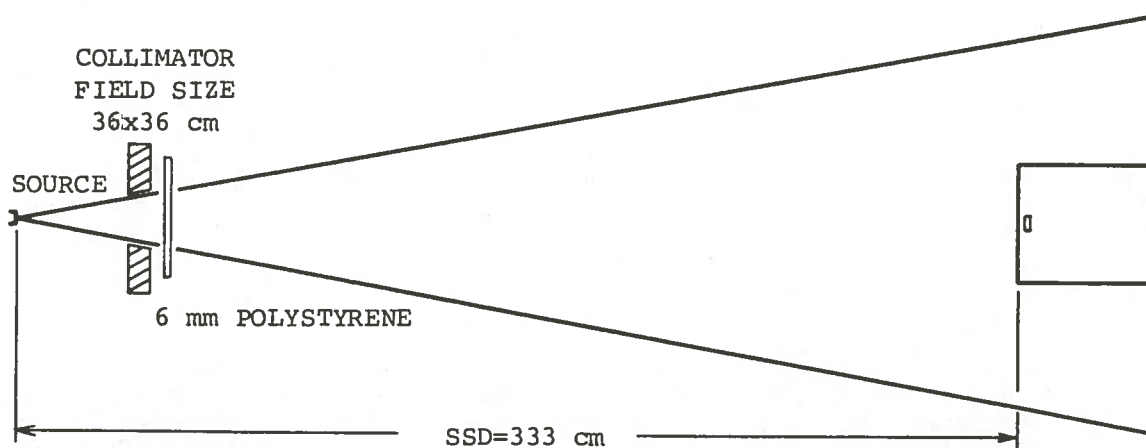


Fig. 8.  Diagram of modified geometry.  The geometry is changed by interposing a polystyrene sheet 6 mm thick in the beam.  The sheet is attached to the collimator face.

SSD=333 cm

300 cm

COLLIMATOR
FIELD SIZE
36x36 cm

SOURCE

POLYSTYRENE
DEGRADER
6 mm THICK
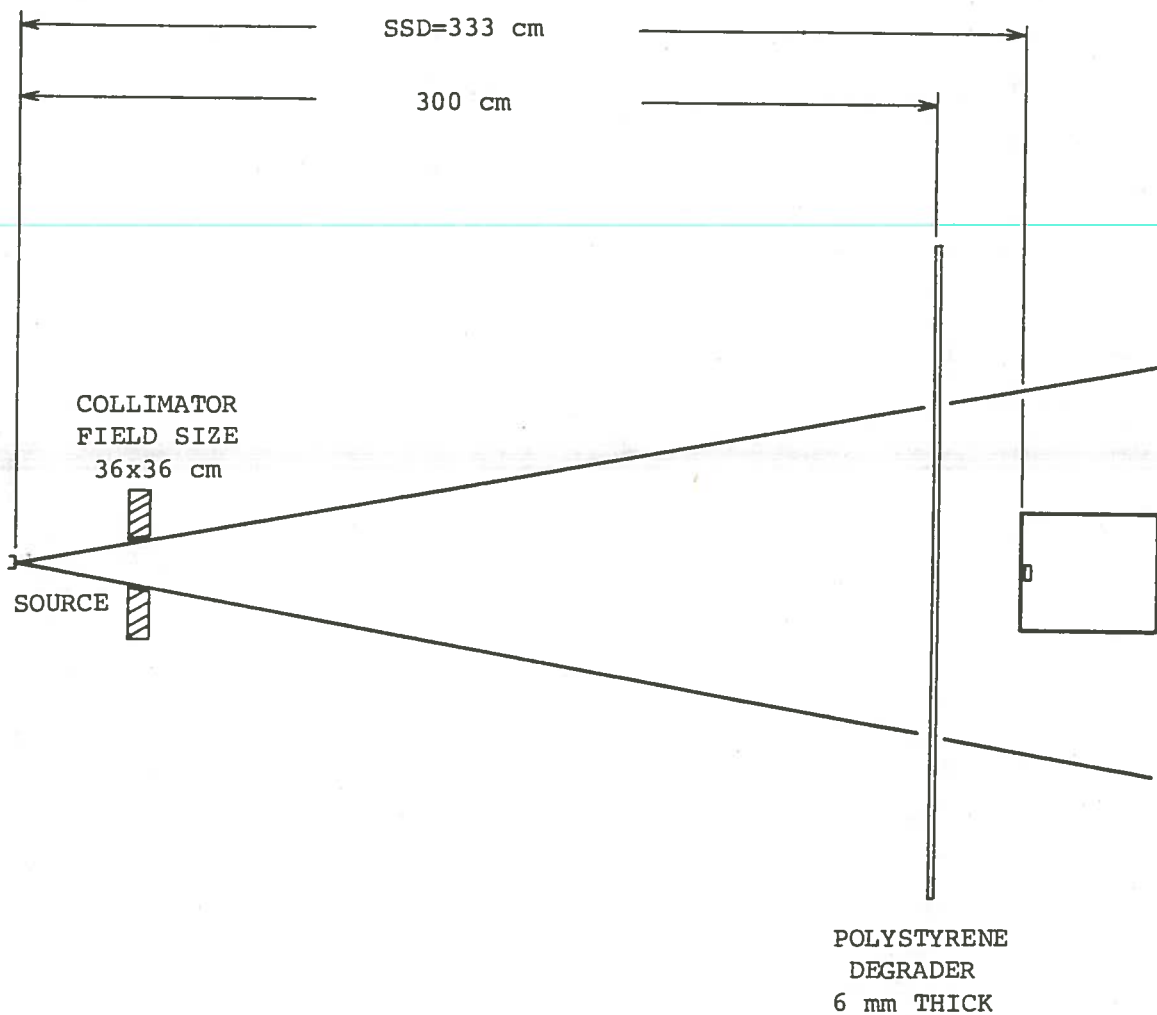
Fig. 9. Diagram of modified geometry. Polystyrene at the collimator
face has been removed. A polystyrene panel 6 mm thick is positioned
in front of the phantom 300 cm from the source.
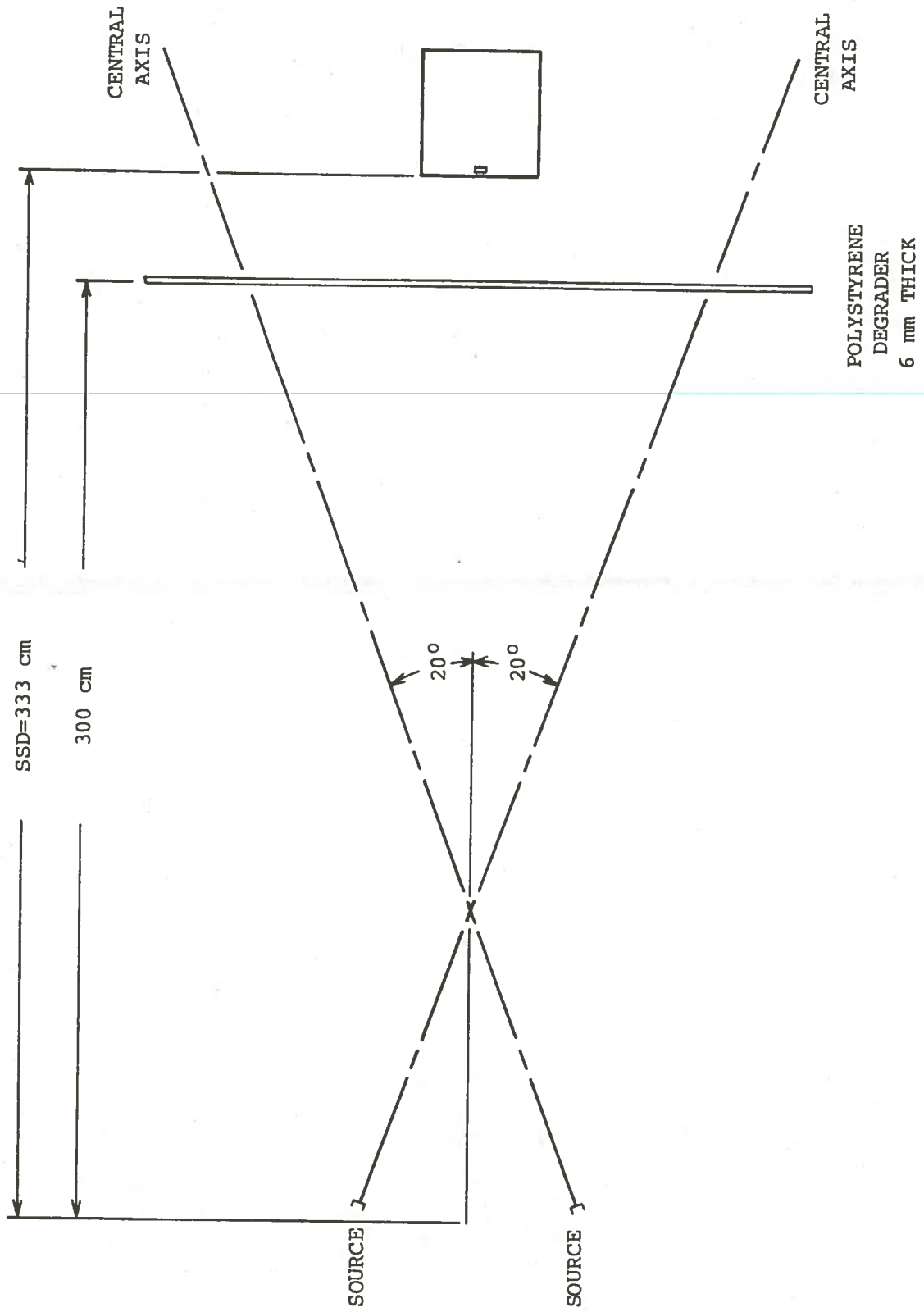
Fig. 10. Diagram of 20° dual-exposure field. Beam is directed alternately 20° above and 20° below the horizontal plane.

All of the geometries illustrated in Figures 3-9 employed a beam directed horizontally towards the phantom. The geometry illustrated in Figure 10, however, did not retain this characteristic. Instead, it simulated the $\pm 20^\circ$ dual-exposure field used in the specialized treatment of mycosis fungoides. The beam was directed alternately $20^\circ$ above and $20^\circ$ below the horizontal (Fig. 10). The 6 mm polystyrene panel was positioned 33 cm in front of the phantom.

## Ionization Measurement System

The primary ionization measurement system included a PTW Electron Beam Chamber (Model No. 23343-291). This chamber is a plane-parallel plate chamber, having a sensitive volume of 0.04 cc (Markus 1973). The chamber is equipped with a protective perspex cap for use in water phantoms. The thickness of the cap is 0.87 mm of perspex which is approximately 1 mm water equivalent.

The chamber was connected to a Keithley Model 616 Digital Electrometer via a shielded triax cable. The cable shield consisted of a galvanized iron pipe 3 meters long having a wall thickness of 4 mm. A polarizing potential of approximately 335 volts was supplied to the chamber by a Keithley Model 6169 Ion Chamber Interface. The Model 6169 Interface is provided with a switchable bipolar bias supply (batteries) to allow for the collection of positive or negative ions.

For an alternate ionization measurement system, the PTW Electron Beam chamber was replaced by a Farmer cylindrical ionization chamber, 0.6 cc sensitive volume. This system was used only for measurement of the ionization values of the standard 10 X 10 cm, 100 cm SSD geometry.

## Relative Ionization Curves

Measurement. A relative ionization curve was measured for each of the geometries listed in the section Experimental Design. The primary ionization measurement system was employed in each one of these measurements. The gantry of the accelerator was rotated 90° from the vertical to provide a horizontally directed beam in all of the geometries except the final ±20° dual-exposure field (which will be discussed later).

The water phantom consisted of a 41 x 41 x 39 cm lucite box equipped with a 20 x 20 cm lucite window, 1.5 mm thick. The phantom, filled with tap water and allowed to stabilize to room temperature, was positioned on the treatment couch for geometries requiring an SSD of 100 cm and on a lightweight cart for geometries requiring an SSD of 333 cm. In each case the crosshairs (central axis) of the field were centered on the ionization chamber within the phantom.

The parallel plate chamber, supported in the phantom by a lucite holder, was positioned directly against the window of the phantom. This placed the point of measurement (the

upper plate) at a depth of 2.5 mm. The chamber was centered on the crosshairs of the field.

Gathering data from an ionization curve entailed making a series of ionization readings, each a result of delivering 200 monitor units (on the machine console) to the measuring system at a rate of 400 monitor units per minute. Measurements were made at one to two millimeter increments from the shallowest depth attainable out to a depth of 5 cm. At each depth, two or three readings were taken with each polarity for a total of four to six readings at each depth. The first reading measured after a change in polarity was always disregarded.

The data for the ionization curve of the $\pm20^{\circ}$ dual-exposure field was gathered in a similar manner. However, at each depth, two sets of measurements were made. One set measured the ionization from the exposure directed $20^{\circ}$ upward and the second set measured the ionization from the exposure directed $20^{\circ}$ downward.

Construction. The ionization readings at each depth for the positive polarity were averaged and readings for the negative polarity were treated likewise. The average of these two polarity values was determined by $(\overline{R}_{+} - \overline{R}_{-})/2$ where $\overline{R}_{+}$ is the average reading at the positive polarity and $\overline{R}_{-}$ is average reading at the negative polarity (Hogstrom 1983).

The average reading at each depth was expressed as a fraction of the maximum reading according to the relationship

$$\text{relative ionization} = \frac{\text{reading at depth}}{\text{maximum reading}}$$

The relative ionization curves were graphed by plotting each relative ionization reading as a function of its depth.

The relative ionization curve for the $\pm 20^{\circ}$ dual-exposure field was determined by first adding the average reading from the exposure directed $20^{\circ}$ upward to the average reading from the exposure directed $20^{\circ}$ downward. The relative ionization values were then determined by dividing the total reading at each depth by the total maximum reading.

Practical range and half-value depth. The practical range of the electrons associated with a particular relative ionization curve is determined by extrapolating the decreasing portion of the curve down to the bremsstrahlung background (Fig. 2). The practical range is the depth at which these two lines intersect. Although the decreasing portion of the curve is linear, a least-squares linear regression was performed to make the best possible extrapolation by a uniform mathematical approach.

The half-value depth is defined as that depth at which the ionization is reduced to 50% (Figure 2). This value is read directly from the relative ionization curve.

## Energy Determination

The energy of an electron beam associated with a particular ionization curve was determined according to guidelines set forth by the International Commission on Radiation Units and Measurements, the Hospital Physicists' Association, and the Nordic Association of Clinical Physics. Each method utilizes an empirical relationship between either the average energy at the surface of the phantom ($\overline{E}_0$) and the half value depth (HVD) or between the most probable energy at the surface of the phantom ($E_{p,0}$) and the practical range ($R_p$).

Most probable energy. For the determination of the most probable energy at the phantom surface, ICRU Report No. 21 (1971) recommends use of the empirical relation

$$\rho \ R_p = k_1 E_{p,0} - k_2$$

where $\rho$ is the density of the medium, $k_1$ is a constant equal to 0.521 $gcm^{-2}$ $MeV^{-1}$ for water and $k_2$ is a constant equal to 0.376 $gcm^{-2}$ for water.

Rearrangement of the equation and substitution of the constant and density values establishes the relationship

$$E_{p,0}(MeV) = 1.92 \ R_p + 0.722$$

The practical range of a 6 MeV standard 10 x 10 cm field, 100 cm SSD is equal to 2.45 cm. Therefore,

$$E_{p,0}(MeV) = (1.92)(2.45) + 0.722$$

$$= 5.4 \text{ MeV}$$

Nordic Association of Clinical Physics (1980) recommends the use of the relationship

$$E_{p,0} = C_1 + C_2 R_p + C_3 R_p^2$$

for energy determination in the range of 1 MeV to 50 MeV, where

$C_1 = 0.22$ MeV, $C_2 = 1.98$ MeV $cm^{-1}$ and $C_3 = 0.0025$ MeV $cm^{-2}$

Using the practical range for the 6 MeV standard 10 x 10 cm field:

$$E_{p,0} = 0.22 \text{ MeV} + (1.98 \text{ MeV } cm^{-1})(2.45 \text{ cm})$$

$$+ (0.0025 \text{ MeV } cm^{-2})(2.45 \text{ cm})^2$$

$$= 5.1 \text{ MeV}$$

Average energy. For the determination of the average energy at the phantom surface the Hospital Physicists' Association (1975) recommends the use of the expression

$$E_0 = 2.37 \text{ HVD} + 0.19$$

where HVD is the half-value depth measured in polystyrene. When the HVD is measured in water, the equivalent depth of polystyrene must be determined. The factor which converts water depth to polystyrene depth is 1.031.

The HVD of the standard 10 X 10 cm field, 100 cm SSD is equal to 1.9 cm. This value, converted to depth in polystyrene, is 1.96 cm. Therefore, according to HPA

$$E_0 (MeV) = 237\ HVD + 0.19$$

$$= 2.37\ (1.96) + 0.19$$

$$= 4.8\ MeV$$

Nordic Association of Clinical Physics (1980) recommends that the average incident energy of an electron beam in MeV, be determined by multiplying the depth of the 50% value of the relative ionization curve by 2.33 MeV/cm. Therefore

$$\overline{E}_0 = 2.33\ HVD$$

Since the HVD for the 6 MeV, standard 10 X 10 cm field, 100 cm SSD is equal to 1.9 cm, according to NACP

$$\overline{E}_0 = (2.33\ MeV\ cm^{-1})(1.9\ cm)$$

$$= 4.4\ MeV.$$

## RESULTS

To evaluate the integrity of the PTW plane-parallel plate chamber, a simple comparison was made to a Farmer cylindrical chamber. The Farmer chamber, though not currently recommended for the measurement of low-energy electron beams, was chosen for the comparison because it has been widely used and has a long history of reproducible exposures. The data plotted in Figure 11 demonstrate the similarity in the relative ionization curves of the Farmer and the PTW chambers for a 6 MeV, 10 X 10 cm field at 100 cm SSD. It is noted that with both chambers the maximum ionization was measured at a depth of 1.00 cm. The practical ranges appear to coincide as do the half-value depths. This comparison, though informal, indicates that the parallel plate chamber functions in a dependable and predictable manner. This chamber was therefore employed in all other measurements carried out in this study.

Figure 12 is a representation of the relative ionization curves produced by the three open field geometries measured at 100 cm SSD. Except for the buildup region, the curves appear to coincide. This indicates that the practical range, the half-value depth and the energy values should be the same for each geometry. Table 1

24
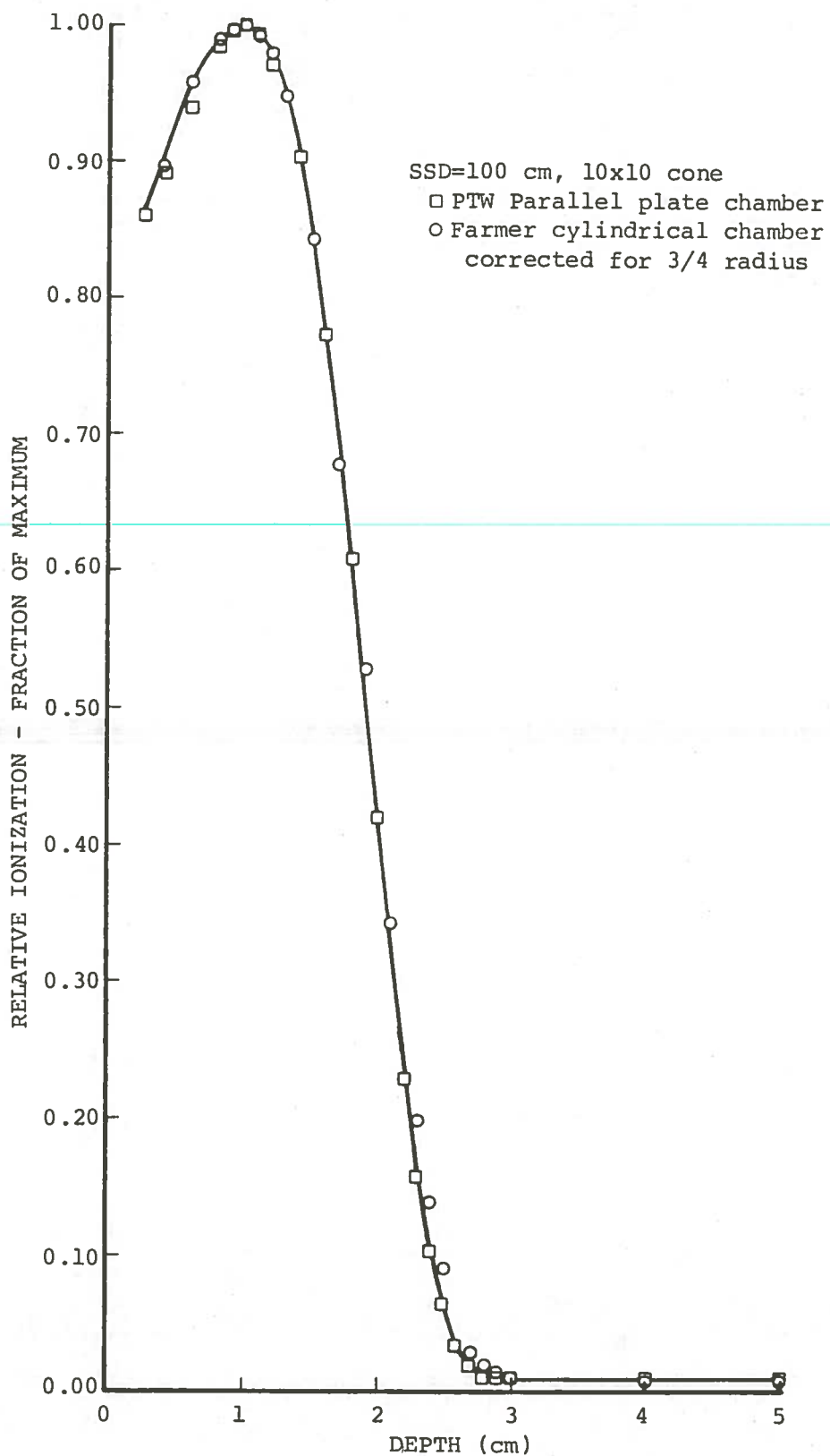
Fig. 11. Comparison of relative ionization data for the PTW plane-parallel plate chamber (0.04 cc sensitive volume) and the Farmer cylindrical chamber (0.6 cc sensitive volume).

SSD=100 cm, OPEN FIELD
□ 10x10 cm cone, 15x15 cm collimator
△ Cone absent, 15x15 cm collimator
○ Cone absent, 36x36 cm collimator
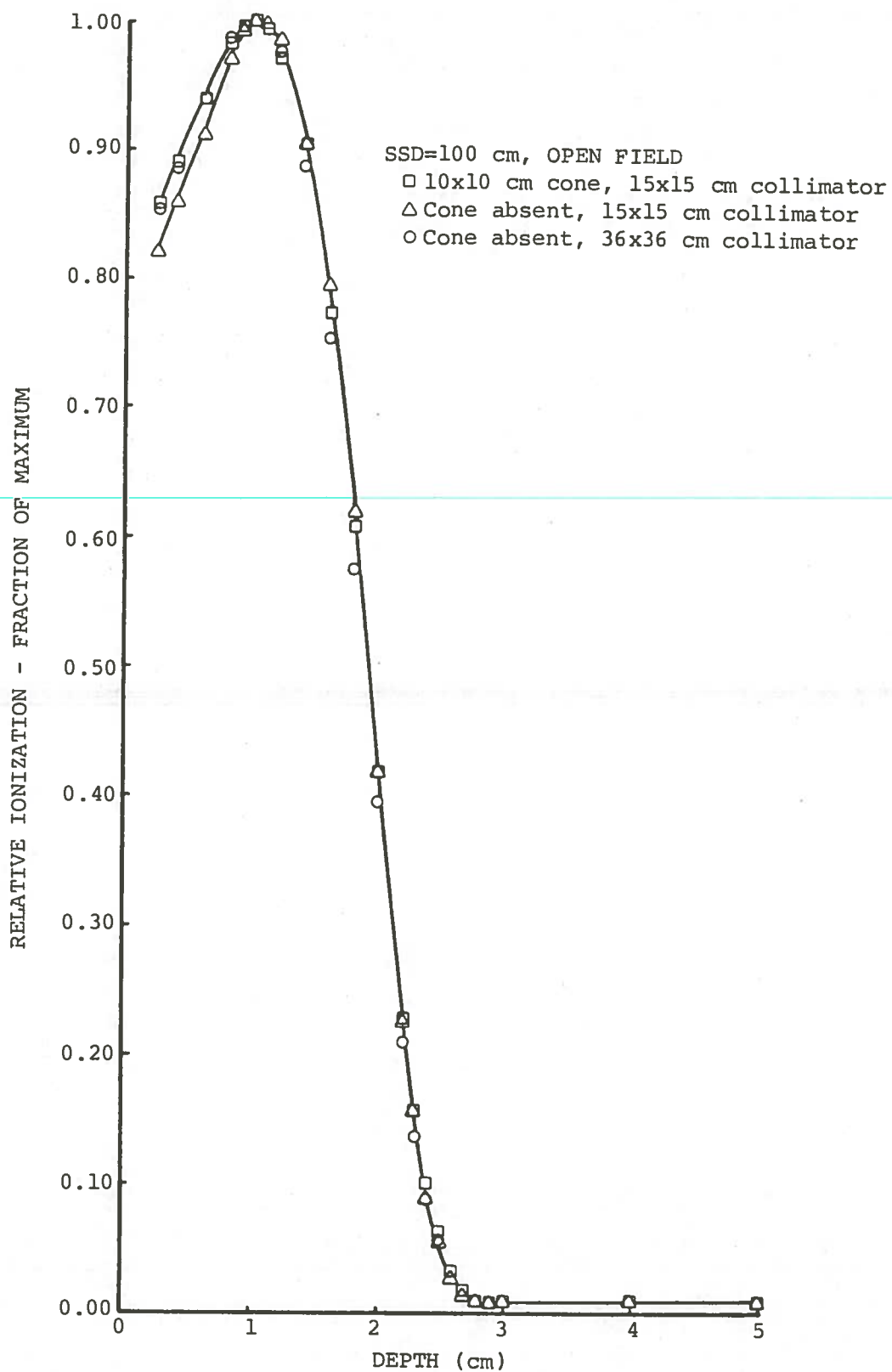
Fig. 12. Change produced in relative ionization by removing the 10x10 cm cone and opening the collimators to full field.

Table 1. Depth of maximum ionization, practical range, half-value depth and energy values for each geometry at the source-surface distance of 100 cm.

| BEAM GEOMETRY | $R_{100}$ (cm) | $R_p$ (cm) | HVD (cm) | $E_{p,0}$ ICRU (1971) | $E_{p,0}$ NACP (1980) | $\bar{E}_0$ (MEV) HPA (1975) | $\bar{E}_0$ (MEV) NACP (1980) |
|---|---|---|---|---|---|---|---|
| 10 x 10 cm cone, 15 x 15 cm collimator | 1.00 | 2.45 | 1.90 | 5.4 | 5.1 | 4.8 | 4.4 |
| Cone absent, 15 x 15 cm collimator | 1.00 | 2.44 | 1.91 | 5.4 | 5.1 | 4.9 | 4.5 |
| Cone absent, 36 x 36 cm collimator | 1.00 | 2.44 | 1.89 | 5.4 | 5.1 | 4.8 | 4.4 |
| Polystyrene at collimator face | 0.70 | 1.90 | 1.40 | 4.4 | 4.0 | 3.6 | 3.3 |

lists the practical ranges, the half-value depths and the energy values which have been determined from the individual ionization curves for the three geometries. Since the practical range values are all within 0.1 mm of one another, they are considered to have the same practical range. The half-value depths are also within 0.1 mm of one another. The energy values for the three curves are determined to be equal to within $\pm 0.1$ MeV.

Figure 13 is a comparison of the relative ionization curve for an open field at 100 cm SSD and the curve produced by the same field with a degrader placed at the collimator face. The shift of the ionization curve as a result of the addition of the degrader is clearly demonstrated. The practical range and the half-value depth are decreased by 5 mm. The depth of maximum ionization shifts from 10 mm to 7 mm. The energy values of the degraded beam, listed in Table 1, are 1.0-1.2 MeV lower than that of the open beam.

Figure 14 is an illustration of the change in relative ionization caused by increasing the column of air from 100 cm to 333 cm. A longer column of air affects the relative ionization curve in the same way that the degrader affects the curve. That is, it shifts the curve to a shallower depth. The shift caused by the increased column of air, however, is not as great as that which is caused by the degrader. According to Tables 1 and 2, the depth of
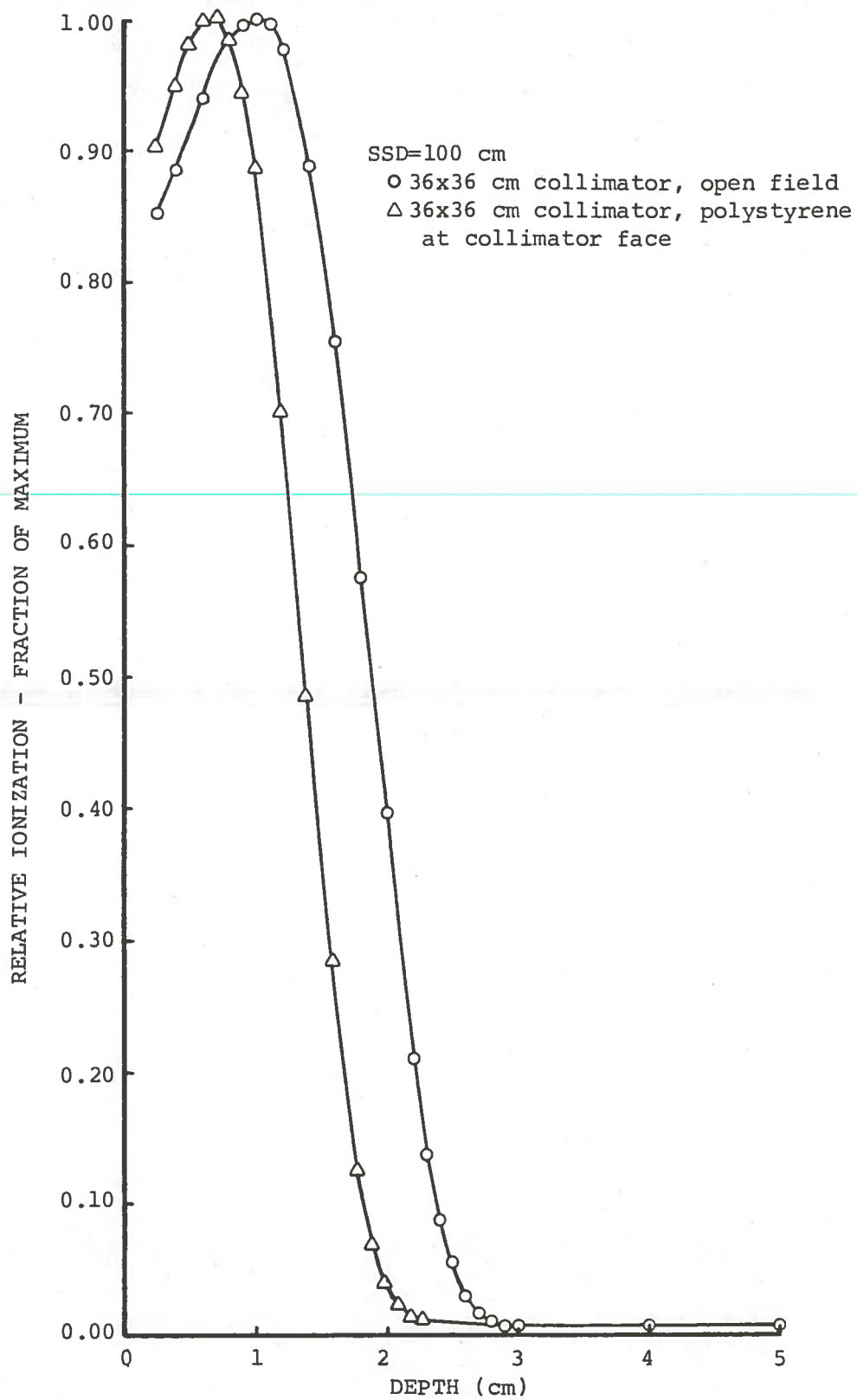
Fig. 13. Change in relative ionization caused by interposing a polystyrene degrader in an electron beam.
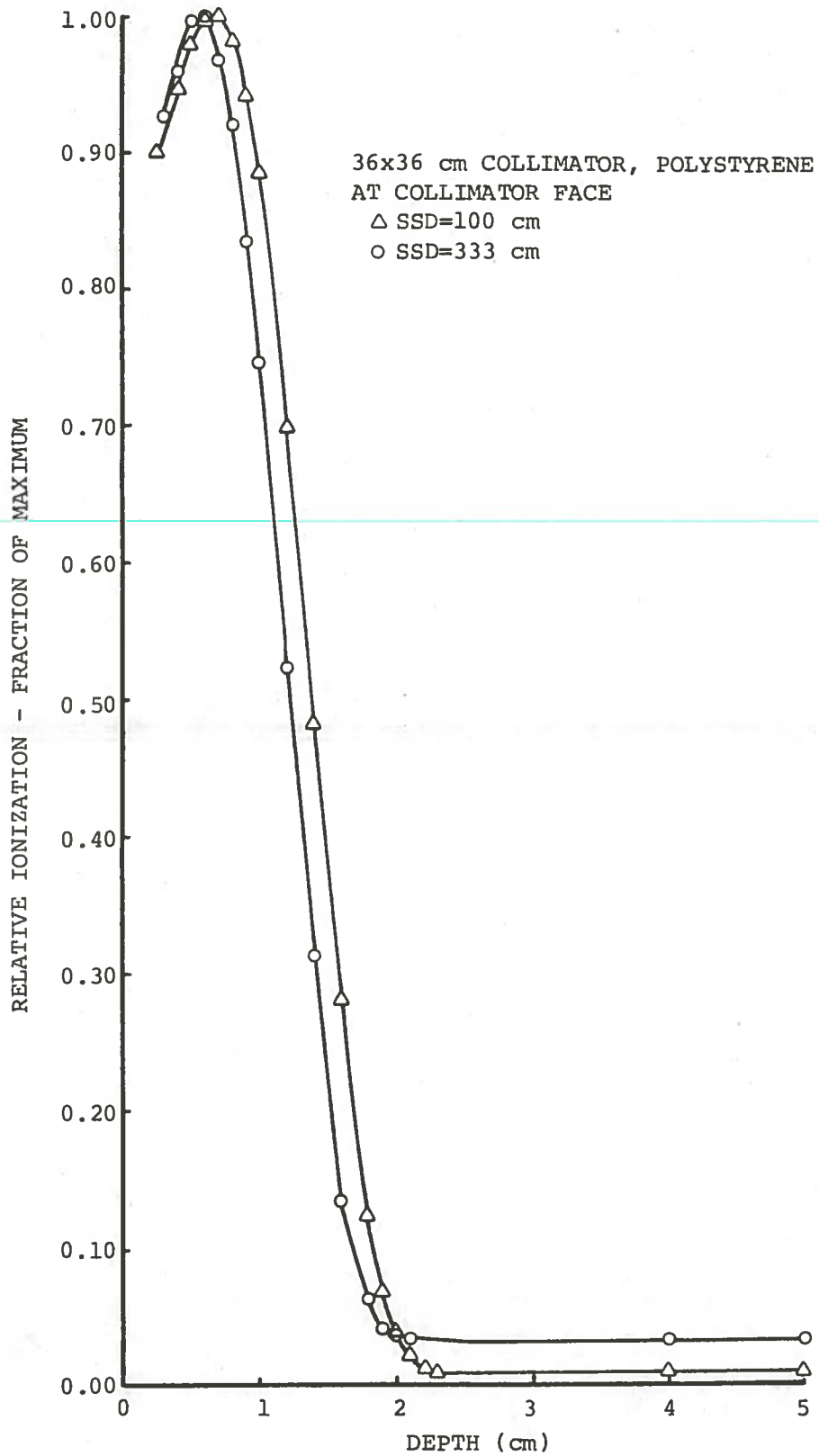
Fig. 14. Change in relative ionization which results from extending the air column.

Table 2. Depth of maximum ionization, practical range, half-value depth and energy values for each geometry at the source-surface distance of 333 cm.

| BEAM GEOMETRY | $R_{100}$ (cm) | $R_p$ (cm) | HVD (cm) | $E_{p,0}$ | | $\bar{E}_0$ (MEV) | |
|---|---|---|---|---|---|---|---|
| | | | | ICRU (1971) | NACP (1980) | HPA (1975) | NACP (1980) |
| Cone absent, 36 x 36 cm collimator | 0.80 | 2.24 | 1.70 | 5.0 | 4.7 | 4.3 | 4.0 |
| Polystyrene at collimator face | 0.60 | 1.70 | 1.23 | 4.0 | 3.6 | 3.2 | 2.9 |
| Polystyrene near phantom | 0.30 | 1.54 | 1.05 | 3.7 | 3.3 | 2.8 | 2.5 |
| 20° Dual-exposure field | 0.30 | 1.51 | 1.05 | 3.6 | 3.2 | 2.8 | 2.5 |

maximum ionization is decreased 1 mm. The practical range and the half-value depth are shifted 2 mm. The energy values are decreased by 0.4 MeV.

Figure 15 is presented to illustrate the change in the relative ionization curve due to the position of the degrader. The curve produced with the degrader near the phantom is shallower than that produced with the degrader at the collimator face. Table 2 indicates that the depth of maximum ionization, the practical range and the half value depth are each decreased 2-3 mm by moving the degrader to a position closer to the phantom. The energy values are decreased by 0.3-0.4 MeV. It is also noted that the photon contamination decreases from 3.5% to less than 1%.

Figure 16 is an illustration of the relative ionization curve for the $\pm 20^{\circ}$ dual-exposure field. Also included on the graph are the curves produced by the single exposures. It is observed that on the composite curve the maximum ionization occurs at a depth of 3 mm. The data in Table 2 indicate that the half-value depth is 1.1 cm and the practical range is 1.5 cm. It is also noted from this table that the energy values determined for the $\pm 20^{\circ}$ dual-exposure field are the same as those determined for the single field directed horizontally towards the phantom.
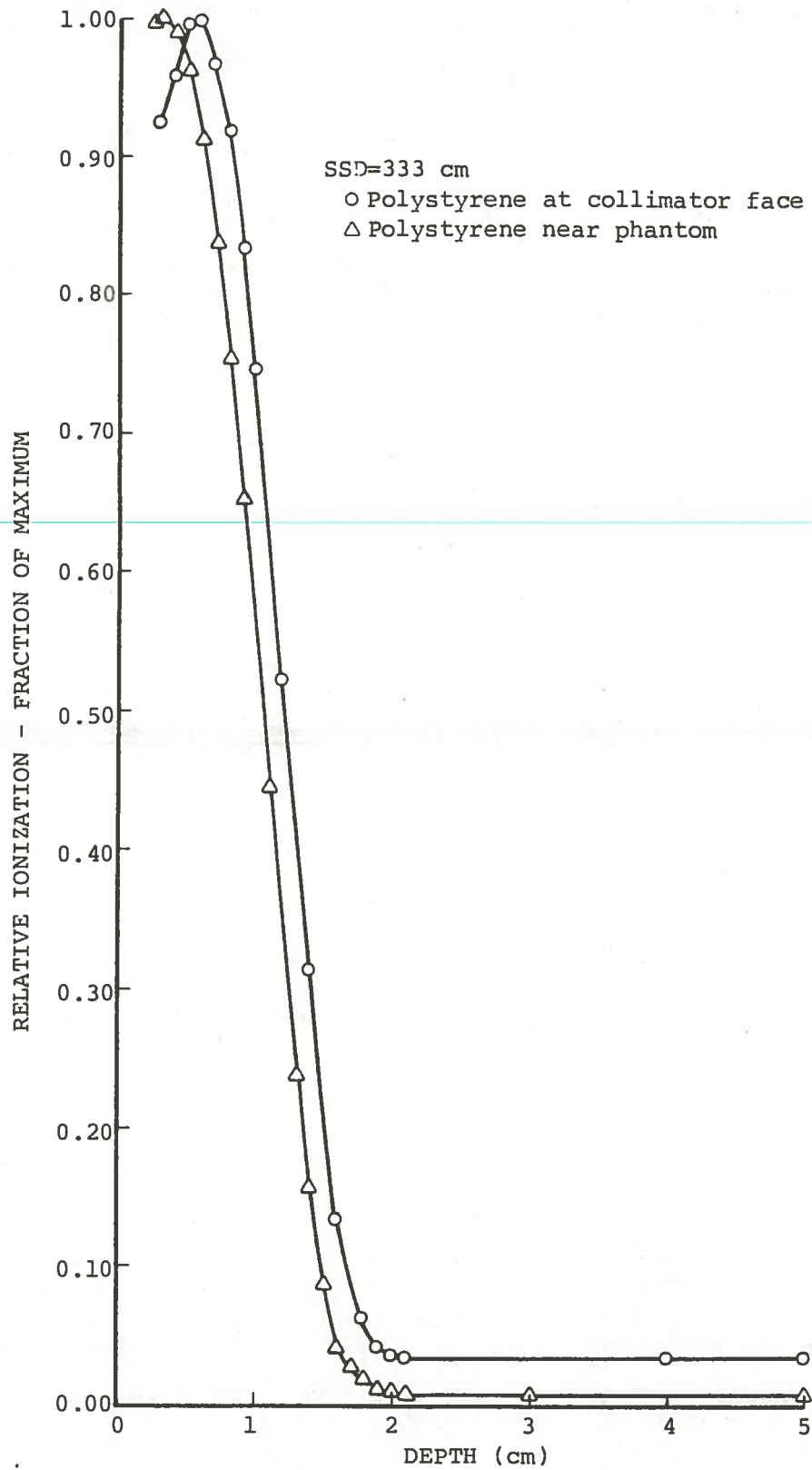
Fig. 15.  Change in relative ionization produced by moving the degrader from the collimator face to a position nearer the phantom.
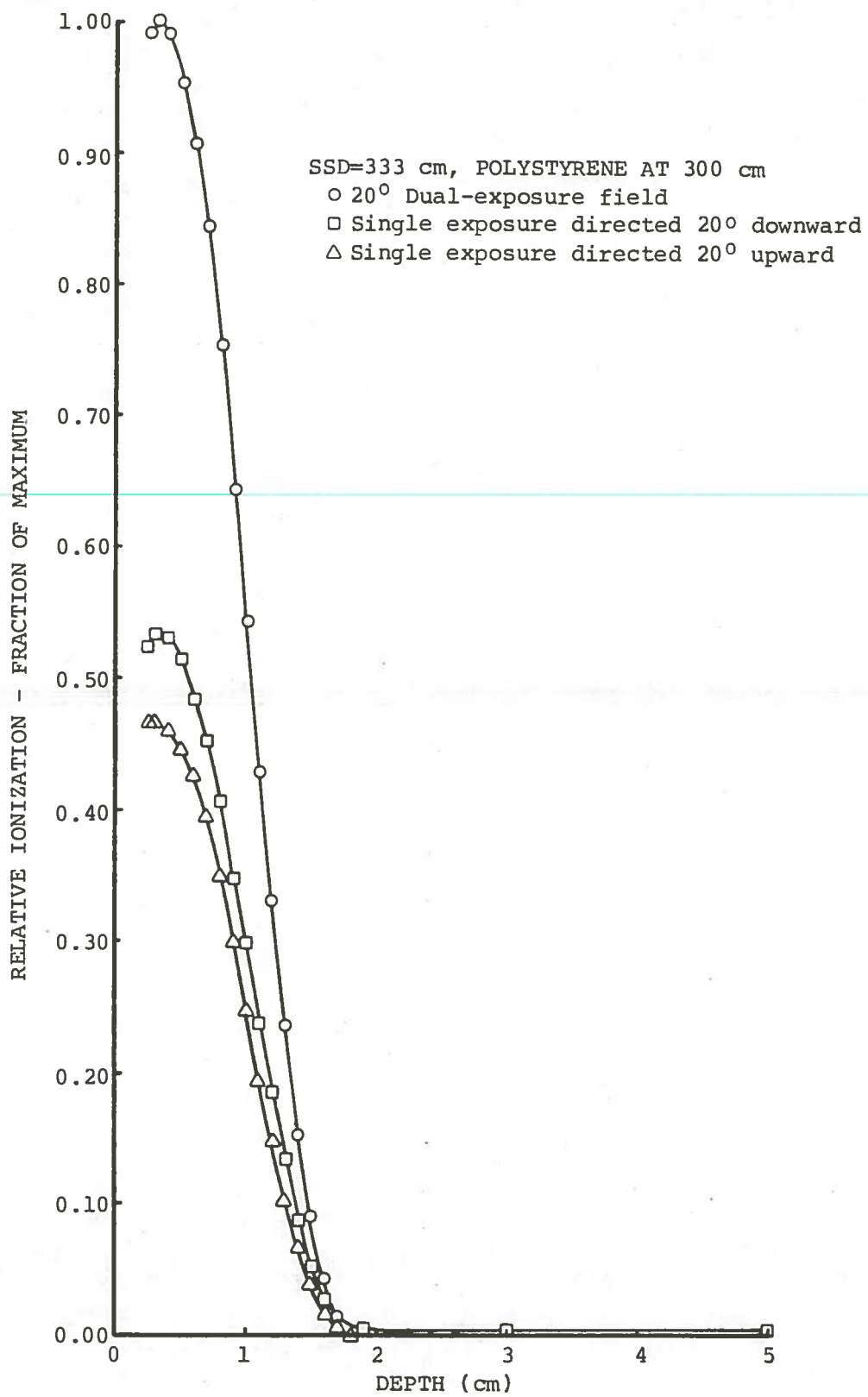
Fig. 16. Comparison of the ionization curves for the single exposures and the 20° dual-exposure field.

## DISCUSSION

From the results presented in the previous section, it is apparent that the changes that have been made in the geometry of the 6 MeV electron beam affect the ionization curve in varying degrees.  Data plotted in Figure 12 indicate that the removal of the cone and the opening of the collimators have essentially no effect on the relative ionization curve and consequently no effect on either the most probable energy or the average energy of the beam. This finding is consistent with that of Karzmark (1960), who found that the inclusion of the collimator extension made no significant changes in the data.

The curves of Figure 12 indicate that, in the buildup region, the relative ionization is reduced slightly when the cone is removed.  The cone, when in position, scatters low energy electrons into the phantom.  These electrons deposit their energy at shallow depths.  When this "source" of scattered electrons is removed the relative ionization in the buildup region decreases.  The relative ionization increases when the collimators are opened to full field.  It is believed that the increase in the diameter of the air column increases the amount of scattering material between

35

the source and the detector. Therefore, more low energy electrons are scattered into the phantom. These low energy electrons serve to increase the relative ionization of the buildup region.

Karzmark (1960) states that, in the beam used to treat mycosis fungoides patients, the 10 foot air path is the major source of energy loss and multiple scattering. The data plotted in Figure 14 demonstrate the shift in the ionization curve due to the extension of the air column from 100 cm to 333 cm. The energy of the beam is reduced by 0.4 MeV. The extension of the air column, however, is not the major source of energy loss with the technique used at the Perkins Radiation Treatment Center.

The change in geometry that has the most dramatic effect on the relative ionization curve is the interposition of a polystyrene degrader in the beam (Fig. 13). A 6 mm thickness can decrease the energy, both probable and average, by as much as 1.5 MeV. Interposition of the polystyrene at the collimator face reduces the energy of the beam by 1.0-1.2 MeV at 100 cm SSD and at 333 cm SSD. Placing the polystyrene near the phantom has an even greater effect. At 333 cm SSD, interposition of the polystyrene reduced the energy by 1.3-1.5 MeV.

Thus, the position of the degrader is also an important factor. The data in Figure 15 demonstrate the decrease in practical range, and therefore the most probable energy, as

a result of moving the degrader from the collimator face out to the front of the phantom. Since the electrons have passed the same amount of material, regardless of the position of the degrader, an explanation must be sought for the decrease in the energy of the beam.

Electrons entering the phantom impinge at many different angles. Since the range of these electrons is measured perpendicular to the phantom surface rather than in the initial direction of the electrons, the effective range of these electrons decreases as their angles of incidence increase (Svensson and Brahme 1981). It is believed that the angular spread, or the range of angles at which the electrons impinge the phantom, is increased with the absorber near the phantom. Therefore a possible explanation for the reduction in the practical range with the absorber near the phantom is the increase in angular spread.

Each of the changes in geometry discussed here has an effect on the formation of the ionization curve of the $20^{\circ}$ dual-exposure field. The optimum combination of these geometry modifications serves to provide a uniform field with the maximum ionization at a depth of 3 mm. The practical range of the electrons is 1.5 cm and the depth at which the ionization is reduced to 50% is 1.0 cm. The most probable energy at the phantom surface is determined to be 3.6 MeV according to ICRU (1971) and 3.2 MeV according to

NACP (1980). The average energy at the phantom surface is determined to be 2.8 MeV according to HPA (1975) and 2.5 MeV according to NACP (1980).

In classifying the energy of the $\pm 20^{\circ}$ dual-exposure field, it was not the intention of this study to determine the most accurate empirical relationship to be used for energy characterization. It was merely to report the values obtained through the application of current protocols. A few comments may be appropriate, however.

The most up-to-date protocol currently available is that of NACP (1980). The equations it recommends for the determination of the energy of an electron beam are reported to provide the best fit to experimental and calculated range-energy values on the low and high energy ranges (Svensson and Brahme 1981). The equation that it recommends for the determination of the average energy at the phantom surface, $\overline{E}_0$ is also recommended by Almond (1981) and is soon to be recommended by the American Association of Physicists in Medicine (AAPM 1983). In light of this, it is felt that best estimation of the most probable energy and the average energy at the phantom surface can be made by employing the range-energy equations recommended by NACP (1980).

One of the purposes of this study was to classify the $\pm 20^{\circ}$ dual-exposure field by a single parameter, namely its energy. It must be pointed out, however, that some authors

have suggested that additional parameters should be used to classify an electron beam (Brahme and Svensson 1976, Almond 1981). These parameters, which characterize the physical properties of the electron beam, include the depth of maximum ionization, the therapeutic range*, and the gradient of the steep section of the absorbed-dose distribution. A more thorough explanation can be found in Brahme and Svensson (1976).

Knowledge of the energy of an electron beam is extremely valuable in that it in necessary for the selection of conversion factors for dosimetry purposes. It is also valuable in the application of standardized depth dose and isodose curves. It is felt, however, that additional parameters such as those defined by Brahme and Svensson (1976) would be useful in making a comparison of the quality of one beam with another. Also from a therapeutic standpoint, it would greatly facilitate definition of the treatment volume.

---

\* The therapeutic range is defined as the depth interval on the absorbed dose distribution that is chosen to enclose the target volume.

# REFERENCES

de Almeida, C. E., and Almond, P. R.. 1973. Letter to the editor. Phys. Med. Biol. 18:737-740.

Almond, P. R. 1981a. Calibration of megavoltage electron radiotherapy beams. In Handbook of Medical Physics, eds. R. G. Waggener, J. G. Kereiakes and R. J. Shalek, CRC Press, Inc., Boca Raton, Fla. pp. 137-180.

Almond, P. R. 1981b. Characteristics of current medical electron accelerator beams. In Proceedings of the symposium on electron beam therapy, eds. F. Chu and J. S. Laughlin, Memorial Sloan-Kettering Cancer Center, New York, NY. pp. 43-53.

American Association of Physicists in Medicine (AAPM). 1966. Protocol for the dosimetry of high energy electrons. Phys. Med. Biol. 11:505-520.

American Association of Physicists in Medicine (AAPM). 1983. A protocol for the determination of absorbed dose from high-energy photon and electron beams. To be published in Med. Phys., Nov.-Dec., 1983.

Brahme, A., and Svensson, H. 1976. Specification of electron beam quality from the central-axis depth absorbed-dose distribution. Med. Phys. 3:95-102.

Hogstom, K. R. 1983. Personal communication.

Hoppe, R. T.; Fuks, Z.; Bagshaw, M. A.. 1979. Radiation therapy in the management of cutaneous T-cell lymphomas. Cancer Treat. Rep. 63:625-632.

Hospital Physicists' Association (HPA). 1975. Report series no. 13, a practical guide to electron dosimetry below 5 MeV for radiotherapy purposes. Hospital Physicists' Association, London.

International Commission on Radiation Units and Measurements (ICRU). 1971. Radiation dosimetry: electrons with initial energies between 1 and 50 MeV. ICRU Publication, Washington, D.C.

Karzmark, C. J.; Loevinger, R.; Steel, R.E.; Weissbluth, M..
1960. A technique for large-field, superficial electron
therapy. Radiology 74:633-643.

Markus, B. 1961. Energiebestimmung schneller Elektronen aus
Tiefendosiskurven. Strahlintherapie 16:280-286.

Markus, B. 1973. Ionization chambers, free of polarity
effects, intended for electron dosimetry.  In Dosimetry
in agriculture, industry, biology and medicine. IAEA,
Wien 1973.

Morris, W. T. and Owen, B. 1975. An ionization chamber for
therapy-level dosimetry of electron beams. Phys. Med.
Biol. 20:718-727.

Nisce, L. Z.; D'Angio, G.; and Kim, J. H. 1973. Weekly
total-skin electron-beam irradiation for mycosis
fugoides. Radiology 109:683-686.

Nordic Association of Clinical Physics (NACP). 1972.
Procedures in radiation therapy dosimetry with 5 to 50
MeV electrons and roetgen and gamma rays with maximum
photon energies between 1 and 50 MeV. Acta Radiologica
Ther. Phys. Biol. 11:603-624.

Nordic Association of Clinical Physics (NACP). 1980.
Procedures in external radiation therapy dosimetry with
electron and photon beams with maximum energies between
1 and 50 MeV. Acta Radiologica Oncology 19:55-79.

Nordic Association of Clinical Physics (NACP). 1981.
Electron beams with mean energies at the phantom suface
below 15 MeV. Acta Radiologica Oncology 20:401-415.

Nüsse, M. 1969. Factors affecting the energy-range relation
of fast electrons in aluminum. Phys. Med. Biol. 14:315-
321.

Page, V.; Gardner, A.; and Karzmark, C. J. 1970. Patient
dosimetry in the electron treatment of large super-
ficial lesions. Radiology 94:635-641.

Schultz, R. J. 1969. AAPM/HPA survey of high-energy electron
depth-dose data. Ann. New York Acad. of Sci. 161:76-
180.

Svensson, H. and Brahme, A. 1981. Fundamentals of electron
beam dosimetry. In Proceedings of the symposium on
electron beam therapy, eds. F. Chu and J. S. Laughlin,

Memorial Sloan-Kettering Cancer Center, New York, NY. pp 17-30.

Svensson, H. and Hettinger, G. 1971. Dosimetric measurements at the Nordic medical accelerators I. Acta Radiologica Ther. Phys. Biol. 10:369-384.

Tapley N., ed. 1976. Clinical applications of the electron beam. John Wiley and Sons, New York, NY. p. 3.

Trump, J. C. et al. 1943. High energy electrons for the treatment of extensive superficial malignant lesions. Radiology 69:623-629.

# VITA

Carrie Ann White was born on February 14, 1958, in Houma, Louisiana. She attended Terrebonne High School in Houma and graduated in June, 1976. In August 1976 she entered Nicholls State University in Thibodaux, Louisiana and graduated with a Bachelor of Science Degree in Science Education in May, 1980. Following graduation she taught high school math in the Terrebonne Parish School System for one year. She entered graduate school in Nuclear Science at Louisiana State University in August 1981. At that time she received a graduate assistantship at the Nuclear Science Center. In May, 1982 her assistantship was transferred to the Clinical Physics Department of the Mary Bird Perkins Radiation Treatment Center. She is currently a candidate for the Master of Science degree in Nuclear Science, Medical Radiation Science Option.

A THERMAL-HYDRAULIC ANALYSIS OF A POOL-TYPE

REACTOR IN NATURAL CIRCULATION

A Thesis

Submitted to the Graduate Faculty of the
Louisiana State University and
Agricultural and Mechanical College
in partial fulfillment of the
requirements for the degree of
Master of Science

in

The Department of Nuclear Engineering

by
Howard A. Brodt
B.S., Louisiana State University, 1980
August, 1983

## ACKNOWLEDGEMENTS

# TABLE OF CONTENTS

Page

# LIST OF TABLES

# LIST OF FIGURES

# ABSTRACT

A proposal to increase the power of the NRAD
reactor at Argonne National Laboratory-West is evaluated
to determine whether the thermal-hydraulic safety limits
would be exceeded.  To do this, a digital computer
program for single-phase and two-phase natural
circulation flow is developed.  The results from this
program indicate that the NRAD proposal is unacceptable,
because void-induced power oscillations are predicted
to be present at the proposed power.

Chapter 1

INTRODUCTION

This thesis is an analysis of the thermal-hydraulics of a low-power research reactor, the Neutron Radiography (NRAD) reactor, at Argonne National Laboratory-West, in Idaho. The reactor is a TRIGA-FLIP reactor designed by General Atomic Company for research and irradiation at power levels up to 2.0 megawatts (MW). The need for this analysis arose in the course of work conducted by Wade Richards of Argonne National Laboratory on a proposal to increase the NRAD power from the present 0.3 MW power to a power of 1.0 MW.

The most important thermal-hydraulic characteristic of the NRAD reactor is that it operates with natural circulation cooling in the core--in other words, the coolant flow in the core is driven solely by the bouancy of the heated water in the coolant channels between the fuel elements. The significance of this fact is that the coolant flow rate through the core depends on the thermal power of the reactor and is influenced by such factors as wall friction and steam produced by nucleate boiling on the fuel element surface. The situation is further complicated by a non-uniform axial heat flux profile. This analysis attempts to

1

model these phenomena, with the goal of predicting the thermal-hydraulic behavior of the NRAD core at present and proposed power levels. Because of the complexity of the problem, a digital computer program was developed to accomplish this goal.

The present NRAD core is composed of fuel elements from the Puerto Rico Nuclear Center (PRNC) reactor which operated in the 1960's. The PRNC reactor was designed to operate at a power of 2.0 MW, but in operation experienced power oscillations at about 1.2 MW.[1]  A likely cause of these power oscillations was the presence of significant steam volume fractions (void fractions) in the high power regions of the core. This problem is discussed in the NRAD safety analysis report, where it was calculated that, for the present 0.3 MW core, an average 0.6% void fraction in the upper half of the nine hottest channels could result in power oscillations of 1%.[2]  Since the NRAD reactor is used for neutron radiography, significant power oscillations are undesirable. The problem of void-induced power oscillations will be considered in this analysis.

The proposed 1.0 MW NRAD power level can be considered acceptable, from a thermal-hydraulic viewpoint, if the following conditions are met:

1)   The maximum fuel element cladding temperature is below the technical specification limit of 1652°F. [3]

2)   The heat flux at all locations is less than the critical heat flux by a certain margin.  The minimum allowable margin can only be determined by statistical methods, and is beyond the scope of this analysis.

3)   Power oscillations are not present.  Void related instabilities are difficult to predict analytically; thus, this analysis will compare the thermal-hydraulic conditions in the 1.0 MW NRAD core to the conditions in the PRNC core at 1.2 MW.  It is assumed that if the NRAD conditions are less severe than those of the PRNC core at the onset of oscillations, then oscillations will not be present in the NRAD reactor.

The following analysis attempts to determine whether the 1.0 MW NRAD core will be able to operate within these limits.

Chapter 2

REACTOR DESCRIPTION

The NRAD reactor is described in this chapter.
Section 1 gives a physical description of the reactor;
the information presented comes from Reference 2.
Section 2 describes the idealized model of a single core
flow channel which is used in Chapter 3 to develop the
thermal-hydraulic equations used in this analysis.

## 2.1. General Description

The NRAD reactor has a core composed of TRIGA-
FLIP fuel elements of 70% enrichment arranged in a square
lattice. There are a total of 61 fuel elements in the
present core; the proposed core will have 80 fuel elements.
The fuel elements are held in clusters of four by upper
and lower end fittings. These end fittings have flow
holes to allow the cooling water easy access to the fuel
element flow channels. A typical cluster is shown in
Figure (2-1). The flow channel formed by the fuel elements
is shown in Figure (2-2). The lower end fitting of each
cluster is fitted into a hole in the grid plate, which
supports the fuel clusters. The core, grid plate, and
core support structure are shown in Figure (2-3).

The NRAD core is contained in an open tank 6.5
feet in diameter, 11.5 feet high, and containing about

4

ALL DIMENSIONS IN INCHES

SECT A A

SECT B B

SECT C C

Locking Plate SECT B B

Locking Nut

2.00 DIA

2.41 DIA

3.00 TYP

1.53 TYP

87 7/8

Lower End Fitting

Upper End Fitting

Lifting Handle

Top Fitting

Upper Reflector

Zirconium Rod

Fuel

Stainless Steel

Lower Reflector

Bottom Fitting

SECT D D

.141 DIA

15

30
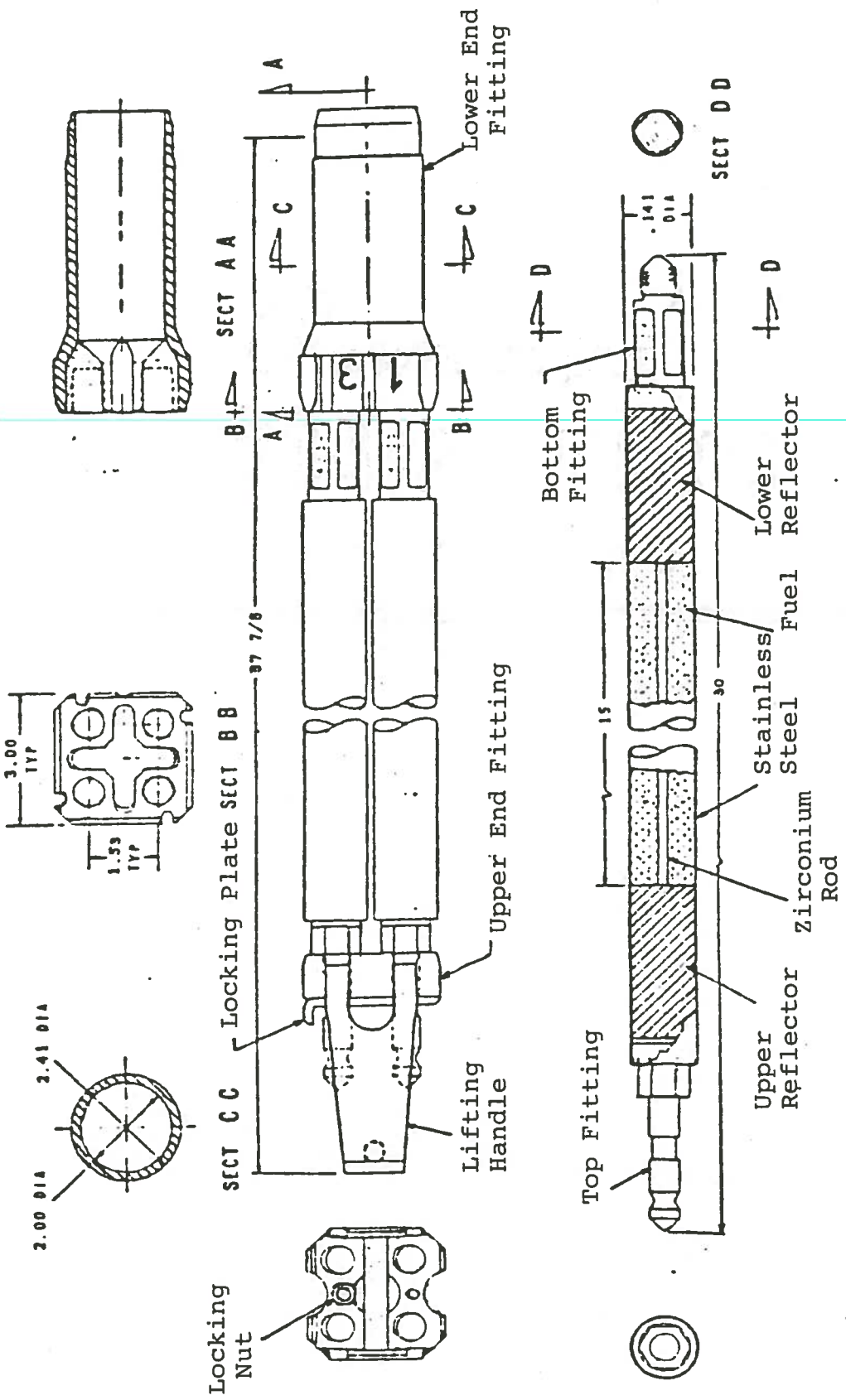
Figure 2-1

Fuel Element Cluster
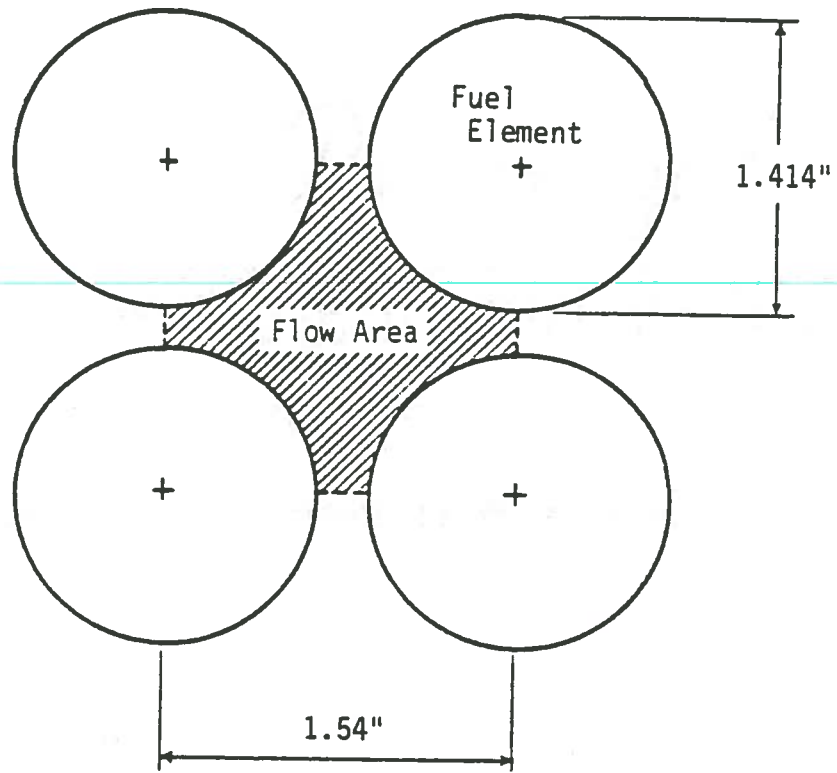
Figure 2-2

Fuel Cluster Flow Channel
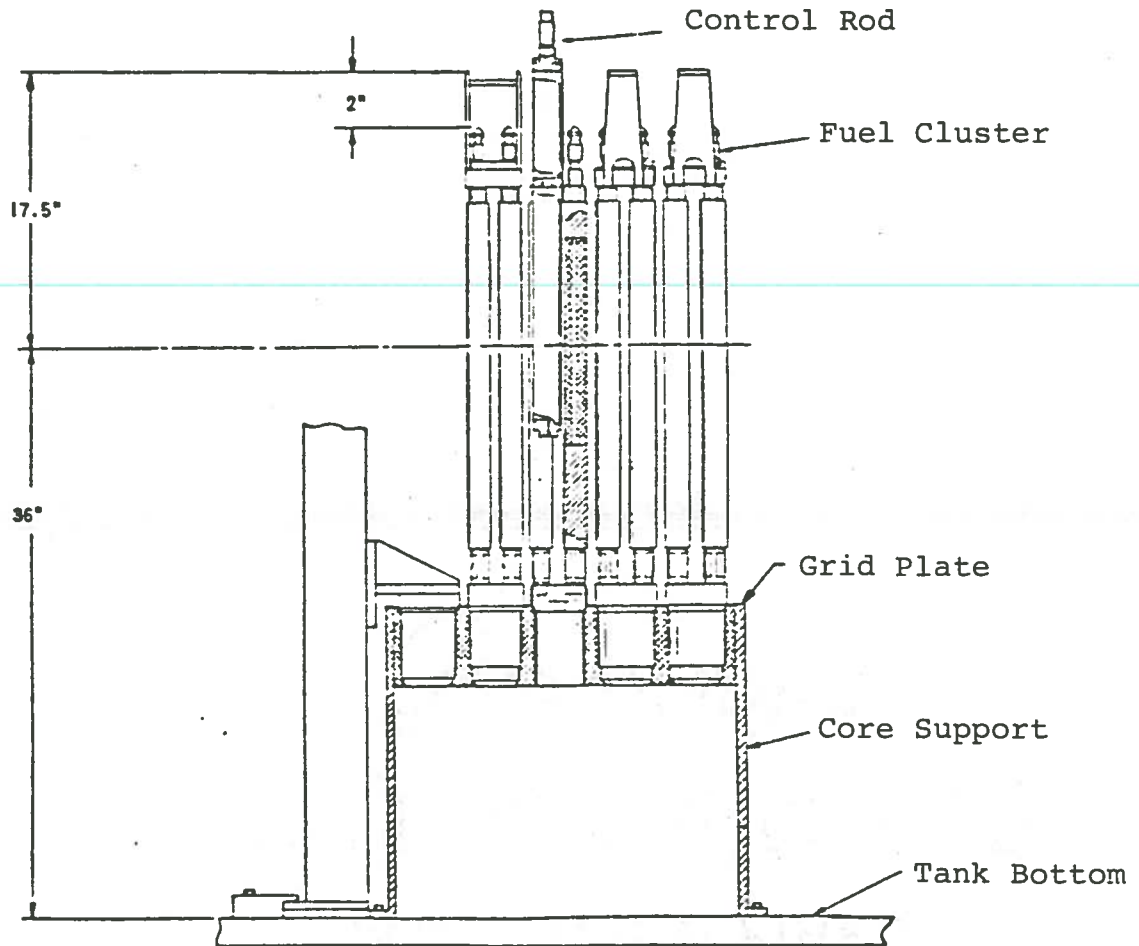
Figure 2-3

NRAD Core and Core Support Structure

2700 gallons of water. The water acts as both a coolant and a moderator for the reactor core. During reactor operation, the thermal power produced in the core is removed by pumping tank water through a heat exchanger to maintain a constant water temperature in the reactor tank. The cooled water is returned to the tank in such a way as to induce a swirl flow pattern in the tank water. The influence of this swirl flow on the flow in the hot channel is unknown, but probably is not important since the hottest channels are in the center of the core. Any effect of swirl flow is neglected in this analysis. The reactor tank is shown in Figure (2-4).

## 2.2. Flow Channel Geometry

For the purpose of this analysis, the coolant flow channel through a fuel cluster is treated as a series of idealized fluid volumes, each described by a vertical length and a flow area. In addition, the fuel rod volumes have a hydraulic diameter and heated perimeter specified; these dimensions are used in friction and heat transfer calculations.

Dimensions for the fuel element volumes are given in Table (2-1). All other dimensions were scaled from the drawing in Figure (2-1). The following volumes were used: two volumes in the lower end fitting (one for each flow area), and one volume each for the bottom fitting of the
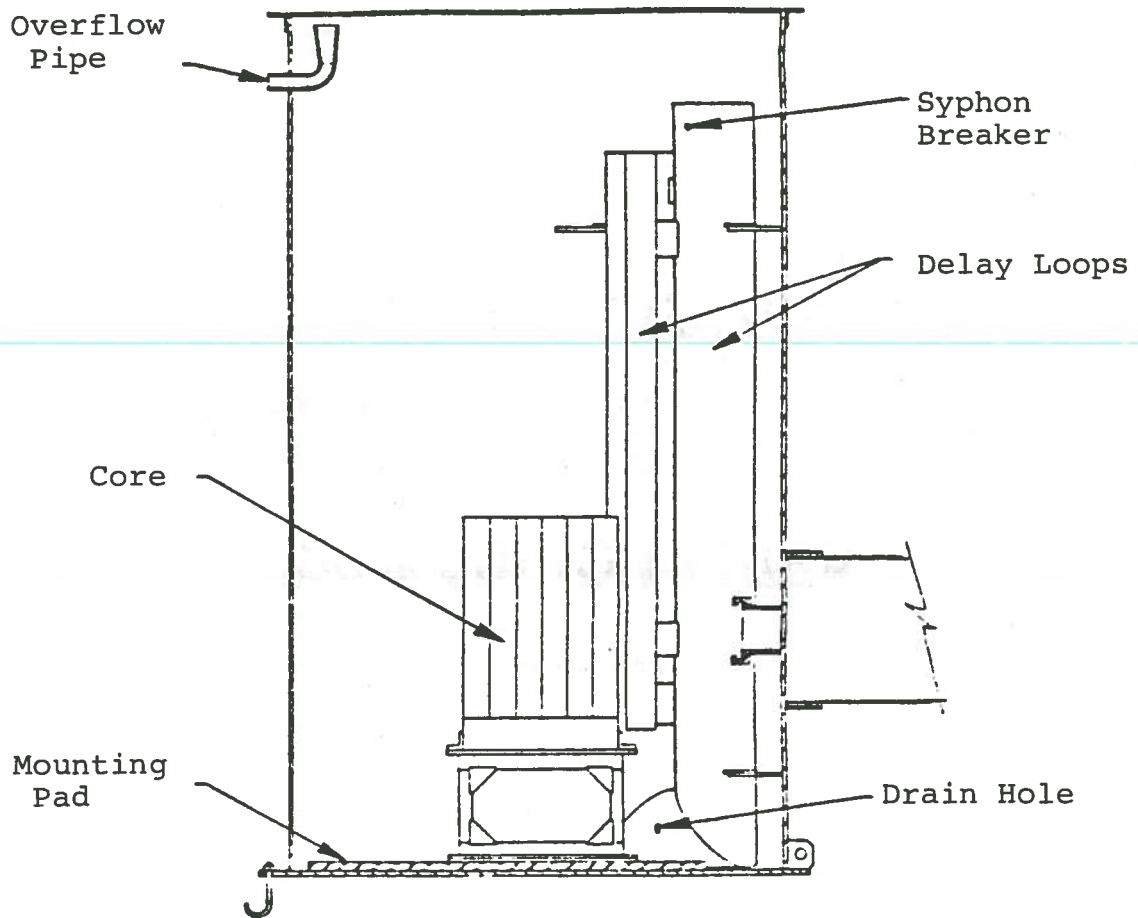
Figure 2-4

NRAD Reactor Tank

Table 2-1

NRAD Fuel Cluster Flow Channel Dimensions

| | |
|---|---|
| Fuel Element Diameter (in) | 1.414 |
| Fuel Element Pitch (in) | 1.53 |
| Heated Length (in) | 15 |
| Flow Area (in$^2$) | 0.769 |
| Heated Perimeter (in) | 4.44 |
| Hydraulic Diameter (in) | 0.694 |

fuel element, the lower reflector, the heated length, the upper reflector, the top fitting of the fuel element, and the upper end fitting. The calculation of local pressure drops at the inlet and outlet to the flow channel also requires the flow area of the reactor tank. The dimensions of these flow volumes are given in Table (2-2). Between each pair of volumes of different flow area is a sudden area change.

Table 2-2

Flow Volume Dimensions

| Volume | Flow Area ($ft^2$) | Flow Length (ft) | Hydraulic Diameter (ft) | Heated Perimeter (ft) |
|---|---|---|---|---|
| Reactor Tank | 32 | -- | -- | -- |
| Lower End Fitting #1 | 0.0218 | 0.438 | -- | -- |
| Lower End Fitting #2 | 0.0141 | 0.118 | -- | -- |
| Bottom Fitting | 0.0108 | 0.1732 | -- | -- |
| Lower Reflector | 0.00534 | 0.3293 | 0.0578 | -- |
| Heated Length | 0.00534 | 1.25 | 0.0578 | 0.37 |
| Upper Reflector | 0.00534 | 0.3475 | 0.0578 | -- |
| Top Fitting | 0.0101 | 0.0625 | -- | -- |
| Upper End Fitting | 0.00545 | 0.1042 | -- | -- |
| Reactor Tank | 32 | -- | -- | -- |

Chapter 3

THERMAL-HYDRAULIC EQUATIONS

This chapter describes the equations used to
calculate the flow channel pressure drop, the wall
temperature and critical heat flux, the liquid subcooling,
and, for two-phase flow, the void fraction. The fluid
flow equations presented here are one-dimensional, steady-
state equations, based on average fluid properties and
velocities over the channel cross-section. (Crossflow
between channels is assumed to be negligible and is not
considered; this is a conservative assumption.)

## 3.1. General Equations

The coolant flow rate, W, in any flow channel in
the core is calculated by finding the flow rate which
gives a total pressure drop through the channel equal to
the elevation, or static, pressure drop in the tank water
over the height of the core. This static pressure drop is
the boundary condition for natural circulation. Since for
natural circulation the dominant pressure drop through the
flow channel is the elevation pressure drop, and the
elevation pressure drop is influenced by the amount of
heating of the coolant in the channel, the flow rate is
different in each flow channel, due to the difference in

13

power in each channel. The hottest, or limiting, channel is investigated in this analysis, since this is the channel where the most severe thermal-hydraulic conditions will occur.

The national circulation condition described above can be stated as follows:

$$\Delta p_{tot} = \rho_{avg} \frac{g}{g_c} H_{core}. \qquad (3\text{-}1)$$

Here $\Delta p_{tot}$ is the calculated total pressure drop through the flow channel, $H_{core}$ is the total height of the core, $\rho_{avg}$ is the average tank water density in the height $H_{core}$, g is the acceleration due to gravity, and $g_c$ is the gravitational conversion factor. The total pressure drop can be broken into three parts:

$$\Delta p_{tot} = \Delta p_{in} + \Delta p_{LH} + \Delta p_{out}, \qquad (3\text{-}2)$$

in which $\Delta p_{in}$ is the pressure drop in the inlet region, including the lower reflector, $\Delta p_{LH}$ is the pressure drop in the heated length, and $\Delta p_{out}$ is the pressure drop in the outlet region, including the upper reflector. Because of the wide variation of liquid temperature, steam void fraction, and heat flux over the heated length, the heated length is broken into increments of equal length

$\Delta Z$ and a pressure drop, $\Delta p_i$, is calculated for each increment. The three pressure drop terms in Equation (3-2) are the sums of several pressure drop components, as shown in the following equations:

$$\Delta p_{in} = \Delta p_{e,in} + \Delta p_{f,LR} + \sum_{j=1}^{4} \Delta p_{\ell,j} \quad \text{and} \qquad (3\text{-}3a)$$

$$\Delta p_{out} = \Delta p_{e,out} + \Delta p_{f,UR} + \sum_{j=5}^{7} \Delta p_{\ell,j}, \qquad (3\text{-}3b)$$

where

$\Delta p_{e,in}$ = elevation pressure drop in inlet

$\Delta p_{f,LR}$ = friction pressure drop in lower reflector

$\Delta p_{\ell,j}$ = local pressure drop at area change j

$\Delta p_{e,out}$ = elevation pressure drop in outlet

$\Delta p_{f,UR}$ = friction pressure drop in upper reflector,

and

$$\Delta p_{LH} = \sum_{i=1}^{N} \Delta p_i = \sum_{i=1}^{N} [\Delta p_{e,i} + \Delta p_{f,i} + \Delta p_{a,i}], \qquad (3\text{-}4)$$

where

$\Delta p_{e,i}$ = elevation pressure drop in increment i

$\Delta p_{f,i}$ = friction pressure drop in increment i

$\Delta p_{a,i}$ = acceleration pressure drop in increment i

$N$ = number of increments in heated length.

These pressure drop components are covered in more detail in later sections.

The rise in the liquid temperature in each increment in single-phase flow is calculated from

$$T_{k+1} = T_k + \frac{q_i'' \, P_H \, \Delta z}{W \, C_{p,i}},$$ (3-5)

in which T is the bulk liquid temperature, q" is the local channel heat flux, $P_H$ is the heated perimeter, and $C_p$ is the liquid specific heat. In Equation (3-5), the subscript k and k+1 refer to the lower and upper ends, respectively, of increment i and the subscript i refers to the average of the values at points k and k+1. This notation is retained throughout this chapter. The calculation of the local heat flux, q", is covered in a later section.

## 3.2. Single-Phase Pressure Drop

The elevation pressure drop in single-phase flow is given by the general equation

$$\Delta p_e = \rho \, \frac{g}{g_c} \, L,$$ (3-6)

which is the same as Equation (3-1). Here L is the axial height considered and ρ is the average density over the height L. In the inlet region L is the total length

of the first four volumes (the height from the channel inlet to the beginning of the heated length) and $\rho$ is the density of the inlet water. In the outlet region L is the total length of the last three volumes (the height from the end of the heated length to the channel outlet) and $\rho$ is the density of the coolant leaving the heated length. In the heated length, Equation (3-6) becomes

$$\Delta p_{e,i} = [\frac{\rho_k + \rho_{k+1}}{2}] \frac{g}{g_c} \Delta Z. \tag{3-7}$$

The local pressure drop, $\Delta p_{\ell,j}$, is calculated from[4]

$$\Delta p_{\ell,j} = [\frac{A_j^2}{A_2^2} - \frac{A_j^2}{A_1^2} + e_v] \frac{W^2}{2 \rho_j g_c A_j^2}, \tag{3-8}$$

where

$A_1$ = flow area upstream of area change j

$A_2$ = flow area downstream of area change j

$A_j$ = the smaller of $A_1$ and $A_2$

$e_v$ = irreversible pressure loss coefficient at area change j

$\rho_j$ = liquid density at area change j.

The term

$$\frac{A_j^2}{A_2^2} - \frac{A_j^2}{A_1^2}$$

in Equation (3-8) is the reversible pressure loss
coefficient. It should be noted that $e_v$ is the loss
coefficient corresponding to the velocity in the smaller
flow area. Since the flow in the lower end fitting
supplies four channels, the flow rate used in Equation
(3-8) for the first two area changes is four times W.
The loss coefficients used in this analysis are given
in Table (3-1).

The friction pressure drop in the heated length,
$\Delta p_{f,i}$, is given by

$$\Delta p_{f,i} = f_i \frac{\Delta Z}{D_H} \frac{W^2}{2 \rho_i g_c A_f^2},\qquad (3-9)$$

where

  $f_i$ = average friction factor in increment i

  $D_H$ = hydraulic diameter

  $\rho_i$ = average density in increment i,

  $A_f$ = flow area in fuel rod channel.

This equation and the friction factor equations which
follow are from Reference 5. The friction factor, $f_i$,
includes the effect of wall heating, and is calculated
from the isothermal friction factor, $f_{iso}$, by the equation

$$f_i = f_{iso} \left[\frac{\mu_{w,i}}{\mu_i}\right]^{0.6},\qquad (3-10)$$

Table 3-1

Pressure Loss Coefficients

(Reference 5)

| Area Change # | Upstream Flow Area (ft$^2$) | Downstream Flow Area (ft$^2$) | Loss Coefficient |
|---|---|---|---|
| 1 | 32 | 0.0218 | 0.53 |
| 2 | 0.0218 | 0.0141 | 0.27 |
| 3 | 0.0141 | 0.0108 | 0.23 |
| 4 | 0.0108 | 0.00534 | 0.35 |
| 5 | 0.00534 | 0.0101 | 0.18 |
| 6 | 0.0101 | 0.00545 | 0.31 |
| 7 | 0.00545 | 32 | 1.0 |

in which $\mu_{w,i}$ is the liquid viscosity evaluated at the average wall temperature, $T_{w,i}$, and $\mu_i$ is the liquid viscosity evaluated at the average bulk temperature, $T_i$. Three flow regimes are considered in calculating the isothermal friction factor: laminar flow, transition flow, and turbulent flow. The laminar flow equation is

$$f_{iso} = \frac{64}{Re_i}, \qquad (3-11)$$

where

$$Re_i = \frac{W\ D_H}{A_f\ \mu_i}. \qquad (3-12)$$

The end of the laminar region and the beginning of the transition region is assumed to occur at Re = 2100. Turbulent flow is assumed to begin at Re = 4000. The equation for turbulent flow is

$$f_{iso} = 0.184\ Re_i^{-0.2}. \qquad (3-13)$$

In the transition region, 2100 < Re < 4000, the isothermal friction factor is assumed to vary linearly from the laminar friction factor at Re = 2100 to the turbulent friction factor at Re = 4000. Equation (3-9) is also used to calculate the friction pressure drop in the lower and upper reflector volumes. In this case, the increment

i becomes the particular volume considered and $\Delta Z$ becomes the volume length.

The acceleration pressure drop is given by[6]

$$\Delta p_{a,i} = \frac{W^2}{g_c \, \rho_i \, A_f^2} \, [\frac{1}{\rho_{k+1}} - \frac{1}{\rho_k}].$$   (3-14)

This pressure drop is caused by fluid acceleration due to the decrease in density brought about by heating.

### 3.3.  Steam Quality and Void Fraction

In order to calculate the pressure drop in the two-phase region, the steam quality and void fraction must be calculated.  The method used is a modification of the subcooled void fraction model of Roubani.[7]  This model takes a mechanistic, or phenomenological approach to the subcooled boiling process.  A mechanistic model was chosen because of the non-uniform axial heat flux profile and the shortage of useful experimental data at the low pressures and flow rates characteristic of the NRAD core. The general procedure used is to first calculate the steam quality, considering steam generation at the heated surface and condensation of the steam in the bulk stream, and then to calculate the void fraction from the quality. Since the amount of condensation depends on the amount of steam present, the equations are iterated on quality and void fraction until a solution is reached.  The

following analysis assumes that the vapor phase is at saturation.

The steam quality, X, is defined as

$$X = \frac{W_g}{W},$$  (3-15)

in which $W_g$ is the mass flow rate of saturated steam and W is the total mass flow rate. The void fraction, $\alpha$, is defined as

$$\alpha = \frac{V_g}{V},$$  (3-16a)

where $V_g$ is the steam volume and V is the total mixture volume. At any point in the channel, the void fraction averaged over the channel flow area is

$$\alpha = \frac{A_g}{A},$$  (3-16b)

in which $A_g$ is the flow area occupied by vapor and A is the total channel flow area, $A_f$.

The change in quality in increment i is given by

$$X_{k+1} = X_k + \frac{\Delta Q_{b,i} - \Delta Q_{c,i}}{W\, h_{fg,k}}$$  (3-17)

Here $\Delta Q_{b,i}$ is the amount of heat per unit time in increment i that goes into steam production, $\Delta Q_{c,i}$ is the amount of heat per unit time in increment i that

goes into the liquid through condensation of steam, and $h_{fg,k}$ is the latent heat at point k.  The steam production term, $\Delta Q_{b,i}$, is calculated by the equation

$$\Delta Q_{b,i} = \frac{q_i'' \, \rho_{g,k} \, h_{fg,k} \, P_H \, \Delta Z}{\rho_{g,k} \, h_{fg,k} + C_{p,i} \, \rho_{\ell,i} \, \theta_i}, \qquad (3\text{-}18)$$

where

$\rho_{g,k}$ = vapor density at point k

$C_{p,i}$ = average liquid specific heat in increment i

$\rho_{\ell,i}$ = average liquid density in increment i

$\theta_i$ = average liquid subcooling in increment i.

The liquid subcooling is given by

$$\theta_i = T_{s,k} - \frac{T_k + T_{k+1}}{2}, \qquad (3\text{-}19)$$

in which $T_{s,k}$ is the saturation temperature at point k. In Equation (3-18), two modes of heat transfer at the heated surface are considered:  nucleate boiling and heating of the subcooled liquid which replaces the detached steam bubbles.  Fully developed nucleate boiling is assumed to be present in the two-phase region; thus, heat transfer by single phase convection is not considered.  The condensation term, $\Delta Q_{c,i}$, in Equation (3-17) was modified by using an empirical correlation given by Levinpthal[8] of the form

$$q''_{cond} \, P_H = H_o \, \frac{h_{fg}}{V_{fg}} \, A_f \, \alpha \, \theta, \qquad (3\text{-}20)$$

where $q''_{cond}$ is the steam condensation heat flux, $H_o$ is an empirical constant with units of $1/F°$, and $V_{fg}$ is the difference between the liquid and vapor specific volumes. By making use of the following definition:

$$\Delta Q_c = q''_{cond} \, P_H \, \Delta Z. \qquad (3\text{-}21)$$

Equation (3-20) is transformed into

$$\Delta Q_{c,i} = H_o \, \frac{h_{fg,k}}{V_{fg,k}} \, A_f \, \alpha_i \, \theta_i \, \Delta Z, \qquad (3\text{-}22)$$

where $\alpha_i$ is the average void fraction in increment i. This is the expression used in Equation (3-17) for $\Delta Q_{c,i}$. It should be noted that if the average liquid temperature reaches the saturation temperature, $\Delta Q_{c,i}$ is equal to zero.

The change in the bulk liquid temperature in increment i due to both heating of the subcooled liquid at the heated surface and condensation of steam is

$$T_{k+1} = T_k + \frac{q''_i \, P_H \, \Delta Z + \Delta Q_{c,i} - \Delta Q_{b,i}}{W \, C_{p,i} \, (1-X_i)}, \qquad (3\text{-}23)$$

in which $X_i$ is the average quality in increment i.

The void fraction at point k+1 is calculated from the quality at k+1 by using the Zuber-Findlay drift-flux model.  The following equations are from Lahey.[8]  The void fraction is given by

$$\alpha_{k+1} = \frac{X_{k+1}}{C_{o,k}[X_{k+1} + \frac{\rho_{g,k+1}}{\rho_{\ell,k+1}}(1-X_{k+1})] + \frac{\rho_{g,k+1} A_f V_{gj,k+1}}{W}},$$

(3-24)

where $C_{o,k+1}$ is the void concentration coefficient and $V_{gj,k+1}$ is the drift velocity.  The concentration coefficient is calculated using the correlation of Dix, as follows:

$$C_o = \beta[1 + (\frac{1}{\beta} - 1)^b],$$

(3-25)

where $\beta$ is the steam volumetric flow fraction given by

$$\beta = \frac{X}{X + \frac{\rho_g}{\rho_\ell} (1-X)}$$

(3-26)

and b is given by

$$b = (\frac{\rho_g}{\rho_\ell})^{0.1}.$$

(3-27)

The drift velocity is calculated from

$$V_{gj} = 2.9 \ [\frac{(\rho_{\ell} - \rho_g) \ \sigma \ g \ g_c}{\rho_{\ell}^2}]^{0.25} ,\qquad (3\text{-}28)$$

in which $\sigma$ is the surface tension. In Equations (3-25) through (3-28) the steam quality and fluid properties are evaluated at point k+1, to give $C_{o,k+1}$ and $V_{gj,k+1}$.

The two-phase flow region is assumed to begin at the axial point where steam bubbles produced on the heated surface by nucleate boiling begin to detach and join the bulk liquid flow. This is the point where the steam bubbles begin to add to the bouancy of the coolant. The departure point was determined experimentally by Saba and Zuber to be the point where the subcooling equalled $\theta_d$, where $\theta_d$ is given by

$$\theta_d = \frac{q'' \ D_H}{455 \ k_{\ell}},\qquad (3\text{-}29)$$

in which $k_{\ell}$ is the liquid thermal conductivity.[9] This correlation applies to heat transfer controlled bubble departure, which is characteristic of the low flow rate in the NRAD core. The two-phase flow equations are used in any increment i if nucleate boiling is present and the subcooling at point k+1 is less than $\theta_d$ evaluated at k+1. The test for nucleate boiling is described in a later section.

In any increment where the subcooling is greater than $\theta_d$ and two-phase flow was present in the previous increment, the steam is assumed to condense completely within the increment, with the change in fluid density and wall friction averaged over the length of the increment. Additionally, if the liquid phase is sub-cooled at the end of the heated length, the steam is assumed to condense completely after the calculations in the heated length are completed. Conversely, if the liquid is saturated at the end of the heated length, the quality and void fraction at that point are assumed to remain constant through the rest of the channel length. The increase in liquid temperature due to complete condensation of steam of quality X at point k+1 is calculated by using Equations (3-17) and (3-23), and assuming that $q_i''$, $\Delta Q_{c,i}$, and $X_{k+1}$ are equal to zero and that $X_k$ equals X. These assumptions result in the following equation:

$$T = T_{k+1} + \frac{h_{fg,k+1}}{C_{p,k+1}} X. \qquad (3-30)$$

In Equation (3-30), T is the liquid temperature after the steam condenses and X is the quality of the end of the previous increment. If this condensation occurs in an increment in the heated length, T becomes $T_k$, and the

temperature rise due to heating is added to this
temperature rise.

## 3.4.  Two-Phase Pressure Drop

In two-phase flow, the elevation pressure drop
is calculated by using a two-phase density in place of
the density in Equations (3-6) and (3-7).  The two-phase
density, $\bar{\rho}$, is defined as[8]

$$\bar{\rho} = (1-\alpha)\rho_{\ell} + \alpha\,\rho_{g}. \tag{3-31}$$

The friction pressure drop in two-phase flow is
calculated by using a two-phase friction factor, $f_{TP}$, in
place of the friction factor in the single-phase friction
pressure drop equation, Equation (3-9).  In this case,
Equation (3-9) is used with the assumption that the total
flow is single-phase; in other words, the only change to
Equation (3-9) for two-phase flow is the friction factor.
The two-phase friction factor is the maximum of two
different friction factors.  The first is the subcooled
boiling friction factor, $f_{SCB}$, given by[10]

$$f_{SCB} = \frac{8\,q''\,A_f}{W\,C_p\,(T_w - T)}. \tag{3-32}$$

As in the case of single-phase flow, this friction factor
is averaged over the length of each increment.  Since

Equation (3-32) is for subcooled boiling, it is only used when boiling is present. The second friction factor is a more conventional two-phase friction factor based on a two-phase friction multiplier, $\phi_{fo}^2$. With this second method, the two-phase friction factor is

$$f_{TP} = f \ \phi_{fo}^2, \tag{3-33}$$

where f is the single-phase friction factor from Equation (3-10). The two-phase multiplier used is the Baroczy multiplier, which includes the effects of steam quality, mass flux, and pressure.[11] This multiplier is composed of two parts: the friction multiplier for a mass flux, G, of $10^6$ $lb_m/ft^2$-hr and a correction factor, $\Omega$, for other mass fluxes, where mass flux is defined as

$$G = W/A_f. \tag{3-34}$$

Thus the two-phase multiplier is given by

$$\phi_{fo}^2 = \phi_{fo}^{2\prime} \ \Omega, \tag{3-35}$$

where $\phi_{fo}^{2\prime}$ is the multiplier at a mass flux of $10^6$ $lb_m/ft^2$-hr. Tables (3-2) and (3-3) show the $\phi_{fo}^{\prime}$ and $\Omega$ values used in this analysis; these values are for a pressure of 14.7 psia.

Table 3-2

Two-Phase Friction Multiplier for $G = 10^6 \, lb_m/hr\text{-}ft^2$

| Quality (%) | $\phi_{fo}^2$ |
|:---:|:---:|
| 0 | 1.0 |
| 0.1 | 2.1 |
| 1 | 8.5 |
| 2 | 14 |
| 5 | 32.5 |
| 10 | 63.5 |
| 15 | 100 |
| 20 | 140 |
| 30 | 220 |
| 40 | 300 |
| 60 | 455 |
| 80 | 650 |
| 100 | 890 |

Note: Linear interpolation is used between values in table.

Table 3-3

Two-Phase Friction Multiplier Correction Factor

| Quality (%) | $\Omega$ | |
| --- | --- | --- |
| | $G = 2.5 \times 10^5$ $lb_m/hr\text{-}ft^2$ | $G = 5 \times 10^5$ $lb_m/hr\text{-}ft^2$ |
| 0 | 1.0 | 1.0 |
| 0.1 | 1.38 | 1.2 |
| 1 | 1.38 | 1.285 |
| 5 | 1.27 | 1.2 |
| 10 | 1.48 | 1.285 |
| 20 | 1.48 | 1.27 |
| 40 | 1.345 | 1.2 |
| 60 | 1.233 | 1.15 |
| 80 | 1.125 | 1.085 |
| 100 | 1.0 | 1.0 |

Note:  Linear interpolation is used between values in table.

The acceleration pressure drop in two-phase flow is[12]

$$\Delta p_{a,i} = \frac{W^2}{g_c A_f^2} [V_{k+1}' - V_k'].$$  (3-36)

Here $V'$ is given by

$$V' = [\frac{(1-X)^2}{1-\alpha} + \frac{\rho_\ell}{\rho_g} \frac{X^2}{\alpha}] \frac{1}{\rho_\ell}.$$  (3-37)

For the case where $X_{k+1}$ is zero, $V_{k+1}'$ becomes $1/\rho_{\ell,k+1}$.

If two-phase flow is present in the outlet volumes, the local pressure drop for single-phase flow, Equation (3-8), is multiplied by another two-phase multiplier, $\Phi$, to account for two-phase friction effects in the area change. The multiplier is given by[13]

$$\Phi = [\frac{(1-X)^2}{1-\alpha} + \frac{\rho_\ell}{\rho_g} \frac{X^2}{\alpha}].$$  (3-38)

In this expression, the quality and void fraction are the values at the area change. As with the two-phase friction pressure drop, Equation (3-8) is used with the assumption that the total flow is single-phase.

## 3.5.  Power Distribution and Heat Transfer

In this analysis, the heat flux at the surface of a fuel element is assumed to be a function of axial

position only. For simplicity, axial conduction is not considered. The local heat flux, q", at any axial location, Z, is calculated by multiplying the average surface heat flux of the element, $q''_{avg}$, by the relative heat flux, RHF, defined as

$$RHF = q''/q''_{avg}. \qquad (3-39)$$

Since the heated perimeter of a single fuel element is equal to the heated perimeter of the channel, the average heat flux is

$$q''_{avg} = \frac{Q_{element}}{\pi \, D \, L_H} = \frac{Q_{element}}{P_H \, L_H}, \qquad (3-40)$$

where $Q_{element}$ is the total thermal power in the element and D is the element diameter. The relative heat flux is calculated from the axial peaking factor, $F_Z^Q$, which is defined as

$$F_Z^Q = \frac{q''_{max}}{q''_{avg}} , \qquad (3-41)$$

where $q''_{max}$ is the maximum heat flux on the fuel element surface. Since axial conduction is not modeled, the local surface heat flux is assumed to be proportional to the local power density averaged over the element cross-section; thus, axial peaking factors defined in

terms of surface heat flux and power are equivalent.
The heat flux at location Z, where Z is the axial
distance from the beginning of the heated length, is
given by

$$q'' = F_Z^Q \ q''_{avg} \ \cos \ [\pi(1+A)(Z-L_{H/2})/L_H]. \qquad (3-42)$$

This equation is adapted from an equation by Tong and
Weisman[5] for a chopped-cosine axial heat flux profile.
The chopped-cosine profile is an approximation to the
actual NRAD axial profile, which is shown in Figure
(3-1). In Equation (3-42), A is a factor calculated
from the peaking factor by solving the following equation:

$$F_Z^Q = \frac{\pi(1+A)}{2 \ \sin[\pi/2(1+A)]} \qquad (3-43)$$

for A; this equation is limited to the range $1 < F_Z^Q \leq$
1.57. Equation (3-42) is derived in Appendix B.

The preceding heat flux analysis was developed
for a single fuel element. Since the heated perimeter
of the flow channel is the same as the heated perimeter
of a fuel element, the channel receives approximately
one fourth of the power of each of the surrounding four
elements; therefore, the channel heat flux is actually
the average of the heat fluxes of each fuel element.
The local channel heat flux is calculated by using the
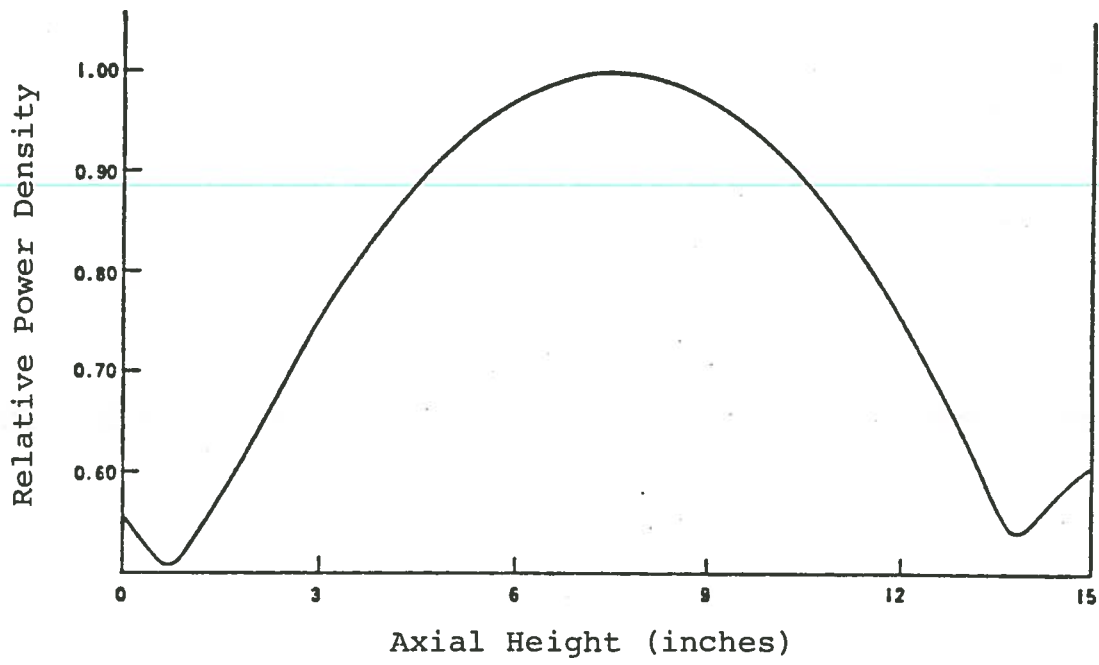
Figure 3-1

NRAD Axial Power Profile

average of the powers of the surrounding fuel elements in place of the single element power, $Q_{element}$, in Equation (3-40). This average element power is also the channel power, $Q_{channel}$. Thus, the channel heat flux can be calculated either from an element power, $Q_{element}$, or from the channel power.

Three heat transfer modes at the heated surface are considered: combined forced laminar convection and natural convection, forced turbulent convection, and nucleate boiling. Nucleate boiling is assumed to be the heat transfer mechanism if the fuel element surface temperature, $T_w$, calculated from the nucleate boiling equation is less than the surface temperature calculated from the appropriate convection equation. This is an approximation to the onset of nucleate boiling region of the boiling curve.

The two convection equations are as follows: for low flow rates (Re less than 2500) the combined convection equation,[4]

$$\frac{H_{SP} D_H}{k_{\ell,f}} = 0.17 \, Re_b^{0.33} \, Pr_b^{0.43} \, \left(\frac{Pr_b}{Pr_w}\right)^{0.25} \, Gr_f^{0.1}$$

(3-44)

is used; for high flow rates (Re greater than 2500) the turbulent forced convection equation,[5]

$$\frac{H_{SP} \, D_H}{k_{\ell,b}} = 0.023 \, Re_b^{\,0.8} \, Pr_b^{\,0.4} \, \left(\frac{\mu_b}{\mu_w}\right)^{0.14} \tag{3-45}$$

is used.  In these equations the variables are

$H_{SP}$ = heat transfer coefficient

Re = Reynold's number

Pr = Prandtl number

Gr = Grashof number,

where

$$Re = \frac{W \, D_H}{A_f \, \mu} \tag{3-46}$$

$$Pr = \frac{\mu \, C_p}{k_\ell} \tag{3-47}$$

and
$$Gr = g\beta\rho^2 (T_w - T) D_H^{\,3}/\mu^2, \tag{3-48}$$

with $\beta$ = coefficient of thermal expansion.

In Equations (3-44) and (3-45), the subscripts b, f, and w refer to properties evaluated at bulk, film, and wall temperatures, where the film temperature is defined as

$$T_f = \frac{T_w + T}{2} . \tag{3-49}$$

The wall temperature in convection is calculated from the heat transfer coefficient and the heat flux by

$$T_w = T + \frac{q''}{H_{SP}} . \tag{3-50}$$

These convection equations are iterated on the wall temperature until a solution is reached.

In the case of nucleate boiling, the wall temperature is given by[14]

$$T_w = T_s + (\frac{q''}{0.074})^{0.259}, \tag{3-51}$$

where $T_s$ is the saturation temperature.

The critical heat flux, $q''_{crit}$, is the heat flux which causes an undesirable increase in wall temperature due to a change in the boiling regime. This temperature excursion can sometimes be great enough to cause failure of the fuel element cladding; hence, critical heat flux is to be avoided in normal operation. The critical heat flux is calculated from the following equations:[15]

$$q''_{crit} = 270 \ D_H^{-0.2} \ (\frac{L_H}{D_H})^{-0.85} \ G^{0.85} \tag{3-52}$$

for G less than 70,155 $lb_m/hr\text{-}ft^2$ and

$$q''_{crit} = 1400 \ D_H^{-0.2} \ (\frac{L_H}{D_H})^{-0.15} \ G^{0.5} \tag{3-53}$$

for G greater than 70,155 $lb_m/hr\text{-}ft^2$. These equations give the minimum critical heat flux in the channel, based on a uniform heat flux throughout the channel. The margin with respect to the critical heat flux is

given by the departure from nucleate boiling ratio, DNBR. This is defined as the ratio of the critical heat flux to the actual heat flux. Since Equations (3-52) and (3-53) are for uniformly heated channels and the NRAD channel has a non-uniform axial heat flux profile, the following approximation for the DNBR in non-uniformly heated channels is used[13]

$$DNBR = 0.85 \ q''_{crit}/q''_{avg}. \qquad (3-54)$$

Chapter 4

PROGRAM DESCRIPTION

The equations in Chapter 3 were coded into a
digital computer program called NAFQ.  This program
calculates the channel flow rate for any channel, given
the channel dimensions, the power to be removed by the
channel, the inlet temperature, and the static pressure
drop in the tank.  To do this, the program iterates on
the channel mass flow rate until Equation (3-1) is
satisfied, within an allowable error.  As given earlier,

$$\Delta p_{tot} = \rho_{avg} \frac{g}{g_c} H_{core}. \qquad (3-1)$$

The static pressure drop given by the right hand side of
Equation (3-1) is input in the form of inlet and outlet
pressures, which form the pressure boundary condition
for the flow rate solution.

To begin the flow rate calculation, an estimate
of the correct flow rate is input; the program then
determines whether to step up or down in flow rate, and
then begins the flow rate iteration, calculating a total
channel pressure drop for each iteration.  When the
pressure boundary condition is satisfied, the results
are printed and the program stops.  For the channel

40

considered, the results printed are the flow rate, the departure from nucleate boiling ratio, the minimum subcooling, and for each axial increment, the bulk liquid, saturation, and wall temperatures, the heat flux, the steam quality, and the void fraction at the increment boundaries.  The overall logic of the program is shown by the flow chart in Figure (4-1), where $\Delta p_o$ is the static pressure drop in the tank.

The major input to the program is shown in Table (4-1).  The following points about several of these input values must be made:

1)  The fluid properties are input in tables of the property as a function of temperature, and linear interpolation is used between table values.

2)  If the radial peaking factor, $F_{XY}^Q$, is input, the element power ($Q_{element}$) for the hottest channel is calculated from

$$Q_{element} = \frac{F_{XY}^Q \times \text{Reactor Power}}{\text{Number of Fuel Elements in Core}} \qquad (4\text{-}1)$$

Alternatively, the channel power ($Q_{channel}$) can be input directly.  The constant used to convert power in megawatts (MW) to power in BTU/hr is $3.4138 \times 10^6$ BTU/hr-MW.[16]
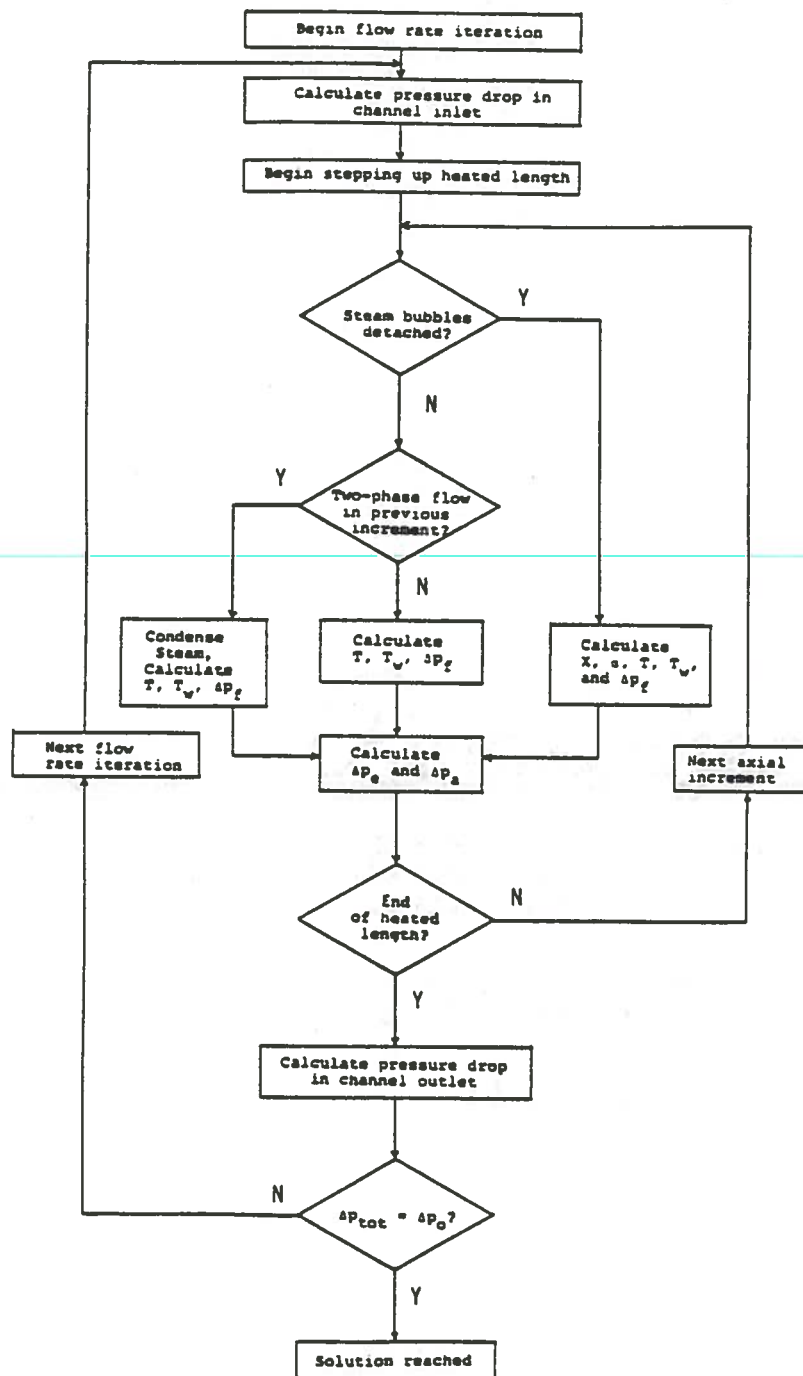
Figure 4-1

Overall Program Logic

Table 4-1

Summary of NAFQ Input

Flow Volume Geometry:
    Flow Area
    Flow Lengths
    Hydraulic Diameter
    Heated Perimeter

Fluid Properties:
    Liquid Density
    Vapor Density
    Liquid Specific Heat
    Liquid Viscosity
    Liquid Thermal Conductivity
    Liquid Thermal Expansion Coefficient
    Surface Tension
    Latent Heat
    Saturation Pressure

Reactor Power

Number of Fuel Elements in Core

Power Factors:
    Axial Peaking Factor
    Channel Power or Radial Peaking Factor

Inlet and Outlet Pressures

Inlet Temperature

Pressure Loss Coefficients

Steam Condensation Coefficient ($H_o$)

Estimate of Steam Quality at the Void Departure Point

Flow Rate Estimate

Allowable Errors:
    Steam Quality
    Wall Temperature
    Flow Rate

3) The value of the steam condensation coefficient was determined from the experimental data of Jordan and Leppert.[17] A description of the method used to determine this coefficient is given in Appendix C.

4) An estimate of the steam quality at the void departure point is necessary to start the void fraction calculation. This quality is $X_k$ in Equation (3-17) for the first increment in two-phase flow. The value of this input variable is chosen to make the void fraction profile smooth at the beginning.

5) The allowable errors are used as convergence tests for the void fraction, wall temperature, and flow rate iterations.

Since significant uncertainties exist in some of these input values, the sensitivity of program results to certain input errors is investigated in the next chapter, where the results of this thesis are presented.

# Chapter 5

## RESULTS

This chapter presents the thermal-hydraulic results from the NAFQ program for the 1.0 MW NRAD design core, along with comparisons of program results to previous analyses and program sensitivity results. All the cases analyzed assume an axial peaking factor of 1.26, which was determined from core neutronics calculations.[2] In all the cases considered, the heat transfer mode from fuel element surface to coolant was fully developed nucleate boiling; thus the convergence error for wall temperature is zero. It should be noted that all of the results presented here represent conditions in the hottest channel.

## 5.1. Comparison to Previous Analyses

In this section, the accuracy of the NAFQ program is investigated by comparing NAFQ results to the results of previous analyses, which are reported in the NRAD final safety analysis report (FSAR).[2] Two comparison cases were performed: a 0.3 MW NRAD core calculation and a 2.0 MW PRNC core calculation. These calculations were also performed in the FSAR. For the comparisons, the input to the NAFQ program was chosen to match the

FSAR conditions as closely as reasonably possible. Since in many cases the assumptions and methods used in the FSAR are not reported, these comparisons are only approximate.

5.1.1. <u>Comparison for 0.3 MW NRAD Case</u>. The input to the NAFQ program for the 0.3 MW NRAD case is shown in Table (5-1). The inlet and outlet pressures were calculated for a tank temperature of 98.6°F, which was measured in the existing NRAD tank at full power.[18] The inlet temperature, radial peaking factor, and number of fuel elements are from Reference 2. The inlet temperature is the water temperature at the inlet to the core flow channel. To make the maximum heat flux calculated by the NAFQ program equal to the FSAR value, the reactor power used was adjusted to 0.312 MW. Since the available computer time was limited, the number of axial increments was chosen as 35, which gives the minimum computer time without sacrificing accuracy. The allowable errors were also chosen to minimize computer time; the quality error, in particular, is relatively large because the void fraction subroutine tends to be slow to converge.

The NAFQ results for this case are compared in Table (5-2) to the calculations from the FSAR. Although the flow rates are much different, the calculation method

Table 5-1

Input for 0.3 MW NRAD Case

| | |
|---|---|
| Inlet Pressure (psia) | 16.302 |
| Outlet Pressure (psia) | 15.086 |
| Inlet Temperature (°F) | 90 |
| Reactor Power (MW) | 0.312 |
| Radial Peaking Factor | 1.59 |
| Axial Peaking Factor | 1.26 |
| Number of Fuel Elements | 60 |
| Number of Axial Increments | 35 |
| Maximum Flow Rate Convergency Error ($lb_m$/hr) | 0.01 |
| Maximum Steam Quality Convergency Error (%) | 1.0 |

Table 5-2

Comparison of NAFQ Results to FSAR
for 0.3 MW NRAD Case

|  | NAFQ | FSAR |
|---|---|---|
| Mass Flow Rate (lbm/hr) | 397 | 518 |
| Maximum Heat Flux (BTU/hr-ft$^2$) | $7.69 \times 10^5$ | $7.67 \times 10^5$ |
| Minimum Subcooling (°F) | 52.1 | 55.8 |
| Maximum Void Fraction (%) | 0 | <0.5 |
| Minimum DNBR | 6.32 | 5.4 |

used in the FSAR is not described, and, therefore, a large uncertainty in this comparison exists. The core temperature rise, as reflected in the minimum subcooling, is nearly the same in both cases, in spite of the large difference in flow rates. This discrepancy appears to exist because the temperature rise was calculated in the FSAR by applying the maximum heat flux to the whole channel length. The NAFQ program predicts single-phase flow throughout the channel; therefore no bubble departure was calculated. Since the void fraction calculated in the NAFQ program is a detached void fraction, a significant amount of attached bubbles could be present on the fuel element surfaces. The void fraction calculated in the FSAR is actually a bounding value; thus, the void fraction agreement between the two calculations is good. The last comparison is for the departure from nucleate boiling ratio (DNBR). Both calculations use the same critical heat flux equation; the reason for the difference in DNBR might be attributed to the way the equations are applied. The critical heat flux given in the FSAR appears to be very conservative.

Although the agreement between NAFQ and FSAR results is not satisfactory for all parameters, the FSAR results seem to be unrealistic and inconsistent. Therefore, a close comparison of these results is not warranted.

5.1.2. Comparison for 2.0 MW PRNC Core. The input to the NAFQ program for the 2.0 MW PRNC case is shown in Table (5-3). The inlet and outlet pressures were calculated for a tank temperature of 110°F.[10] The inlet temperature and number of fuel elements are taken from Reference 2. The radial peaking factor was calculated to give a maximum heat flux equal to that given in the FSAR. The remaining input is the same as in the previous case.

The NAFQ results for this case are compared in Table (5-4) to the calculations from the FSAR. The agreement for this case is better than in the previous case. The FSAR results for this case were calculated by a computer program written by General Atomic. The NAFQ program uses the same general methodology as the General Atomic program; therefore, the differences between the NAFQ and FSAR results for this case are primarily due to differences in the correlations used in each program and in the input. A particular note must be made of the void fraction calculations. The NAFQ void fraction calculation predicts a void fraction which increases with axial height to the end of the heated length; this will be shown in the next section. The General Atomic program, on the other hand, by relying completely on the data of Jordan and Leppert[17] tends to predict a decreasing void fraction in the topmost

Table 5-3

Input for 2.0 MW PRNC Case

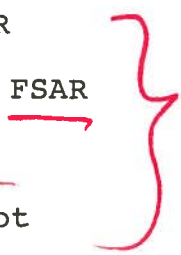| | |
|---|---|
| Inlet Pressure (psia) | 25.157 |
| Outlet Pressure (psia) | 23.945 |
| Inlet Temperature (°F) | 90 |
| Reactor Power (MW) | 2.0 |
| Radial Peaking Factor | 1.54 |
| Axial Peaking Factor | 1.26 |
| Number of Fuel Elements | 95 |
| Number of Axial Increments | 35 |
| Maximum Flow Rate Convergence Error ($lb_m$/hr) | 0.01 |
| Maximum Steam Quality Convergency Error (%) | 1.0 |

Table 5-4

Comparison of NAFQ Results to FSAR
for 2.0 MW PRNC Case

|  | NAFQ | FSAR |
|---|---|---|
| Mass Flow Rate  ($lb_m$/hr) | 797 | 769 |
| Maximum Heat Flux (BTU/hr-ft$^2$) | $3.02 \times 10^5$ | $3.02 \times 10^5$ |
| Minimum Subcooling (°F) | 8.78 | 5.04 |
| Maximum Void Fraction (%) | 10.5 | 6 |
| Minimum DNBR | 2.28 | 1.37 |

part of the heated length, where the void fraction is usually largest. Because of this difference, the maximum void fraction calculated by the NAFQ program is inherently larger than that given in the FSAR, even if the channel average void fractions are the same. In light of this fact, the agreement between the void fraction values in Table (5-4) is good.

Based on the two comparisons given in this section it is concluded that the NAFQ program agrees with the previous analyses to within the modeling, input, and roundoff uncertainties.

## 5.2. Results for the 1.0 MW NRAD Core

Two cases for the 1.0 MW NRAD core were analyzed: a case using the tank temperature and inlet temperature expected to occur with the current heat removal system design and a case which assumes an upgraded heat removal system. The results for these two cases are discussed in this section.

5.2.1. The 1.0 MW NRAD Design Case. The first case considered in this section is the 1.0 MW NRAD design case. This case is a prediction of the thermal-hydraulic conditions in the hottest channel of the NRAD core at a power of 1.0 MW with a tank water temperature of 140°F and an inlet temperature of 120°F. These two temperatures were calculated by the Argonne-West staff,

based on a reactor power of 1.0 MW and the heat removal capacity of the existing heat removal system.[18] This is considered the 1.0 MW NRAD design case.

The NAFQ input for this case is shown in Table (5-5). As in the last section, an axial peaking factor of 1.26 was assumed. The fuel element powers were provided by Mr. Wade Richards of Argonne-West.[18] These powers were computed by workers at Texas A&M University using a core neutronics computer program. Since the channel power was input, it was not necessary to input the number of fuel elements.

The calculated results for this case are given in Table (5-6). The mimimum subcooling and maximum void fraction calculated for this case are approximately the same as these calculated by the NAFQ program for the 2.0 MW PRNC core (Table 5-4). This means that the present 1.0 MW design is likely to experience the same power oscillation problems as experienced with the PRNC reactor. The DNBR is reasonably high, and is larger than that in the PRNC, which never experienced critical heat flux problems.[2] Therefore, this critical heat flux margin should be adequate. Finally, the maximum clad temperature of 259°F is far below the technical specification limit of 1652°F given in Chapter 1.

Table 5-5

Input For 1.0 MW NRAD Case

| | |
|---|---|
| Inlet Pressure (psia) | 16.260 |
| Outlet Pressure (psia) | 15.057 |
| Inlet Temperature (°F) | 120 |
| Reactor Power (MW) | 1.0 |
| Channel Power (KW) | 17.338* |
| Axial Peaking Factor | 1.26 |
| Number of Axial Increments | 35 |
| Maximum Flow Rate Convergence Error ($lb_m/hr$) | 0.01 |
| Maximum Steam Quality Convergency Error (%) | 1.0 |

* Represents the average of the powers of the four fuel elements surrounding the hottest channel; these four power levels are: 16.15, 16.96, 17.11, and 19.13 KW/element.

Table 5-6

NAFQ Results for 1.0 MW NRAD Case

| | |
|---|---|
| Mass Flow Rate $(lb_m/hr)$ | 684 |
| Maximum Heat Flux (BTU/hr-ft$^2$) | $1.61 \times 10^5$ |
| Minimum Subcooling (°F) | 6.82 |
| Maximum Void Fraction (%) | 9.14 |
| Minimum DNBR | 3.95 |
| Maximum Cladding Temperature (°F) | 259 |

The axial variation of the heat flux, bulk
liquid temperature, wall temperature, and void fraction
is shown in Figures (5-1) to (5-4). In these figures,
the axial distance is the distance from the beginning
of the heated length. The increase in void fraction with
axial height can be seen in Figure (5-4).

The results for this case will be compared in
Section 5.3 to the results for the PRNC reactor at a
power of 1.2 MW.

5.2.2. The 1.0 MW NRAD Core with Upgraded Heat
Removal. This case investigates the effects on the
calculated results from Section 5.2.1 of an upgraded
heat removal system for the NRAD reactor. The calculation
presented here was performed by assuming that all the
input parameters from the 1.0 MW NRAD design case were
the same, except for the tank water temperature and the
inlet temperature. For this case, the heat removal
system was assumed to have been upgraded to a capacity
capable of maintaining a 98.6°F tank temperature and a
90°F inlet temperature. These are the temperatures in
the present 0.3 MW NRAD reactor at full power. The NAFQ
input for this case is shown in Table (5-7) and the
calculated results are shown in Table (5-8). As can be
seen in Table (5-8), the maximum void fraction for this
case is much less than in the 1.0 MW NRAD design case.
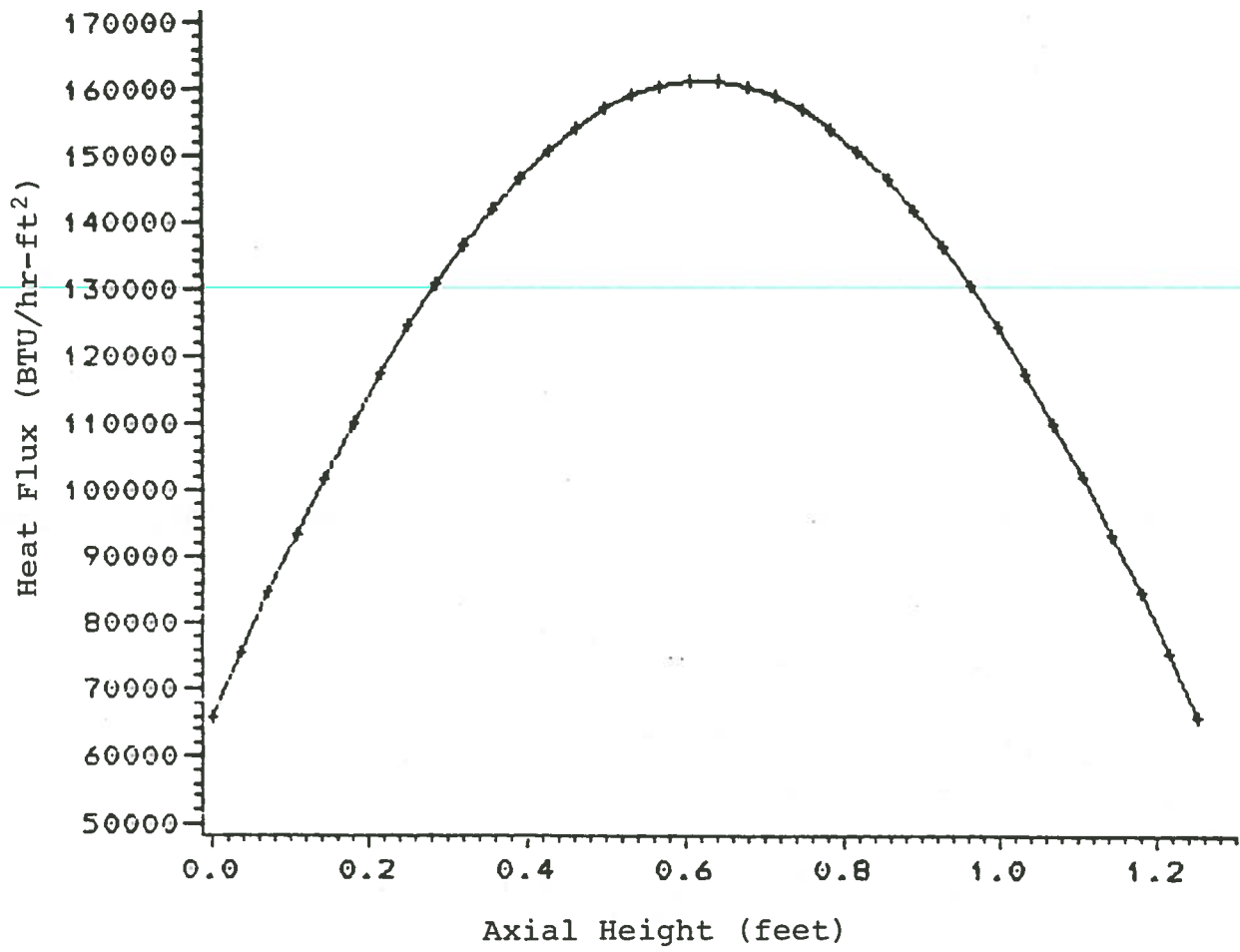
Figure 5-1

Heat Flux Profile
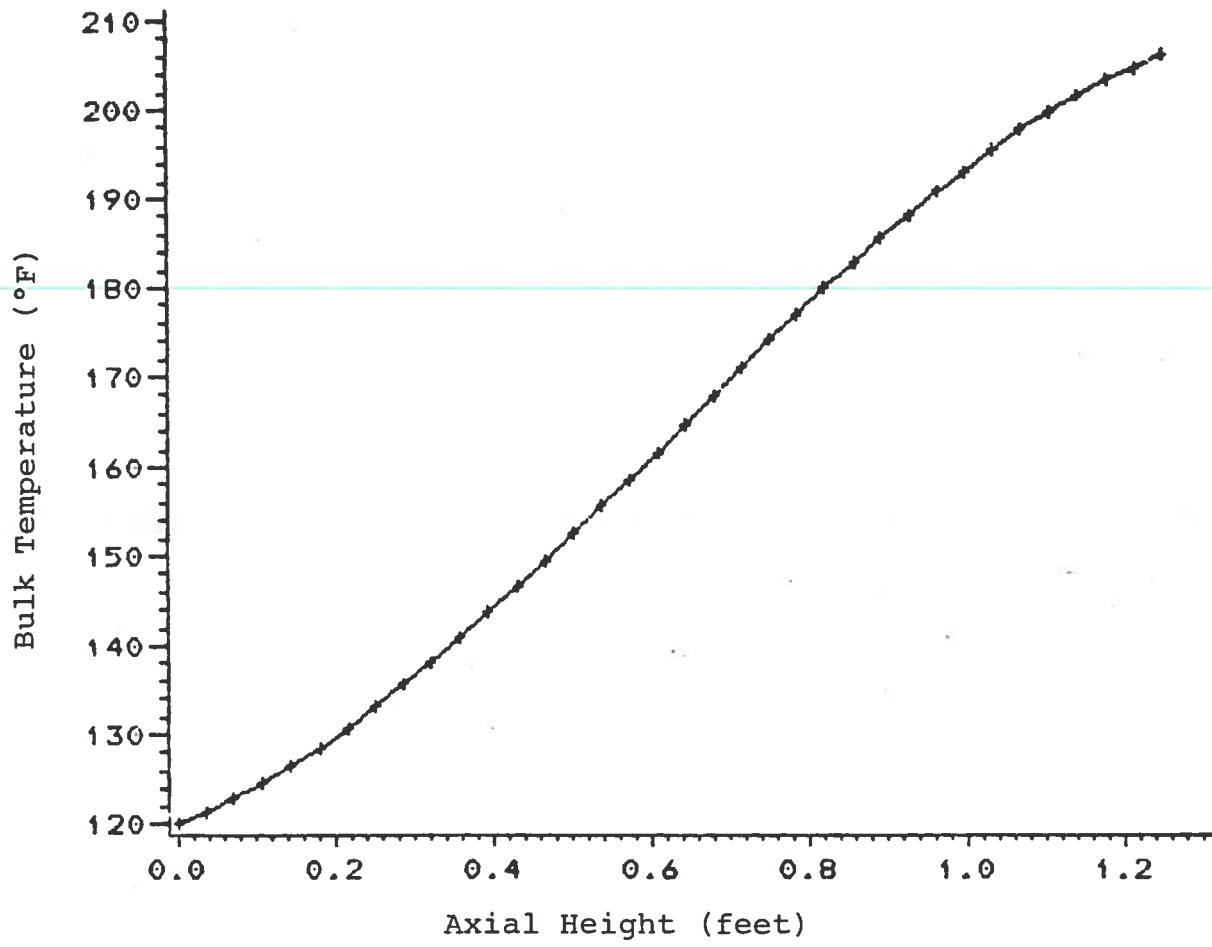
Figure 5-2

Bulk Temperature
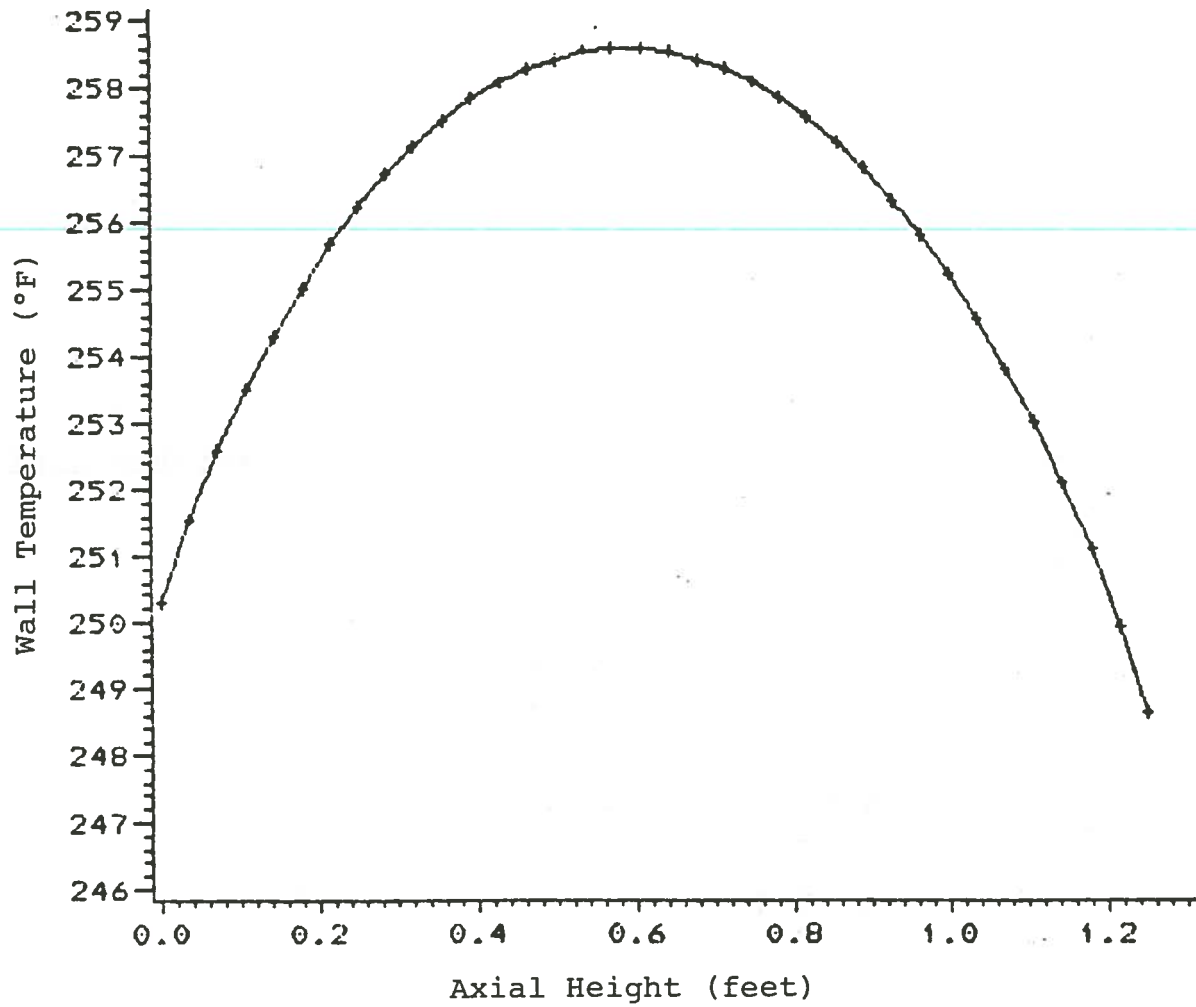
Figure 5-3

Wall Temperature Profile
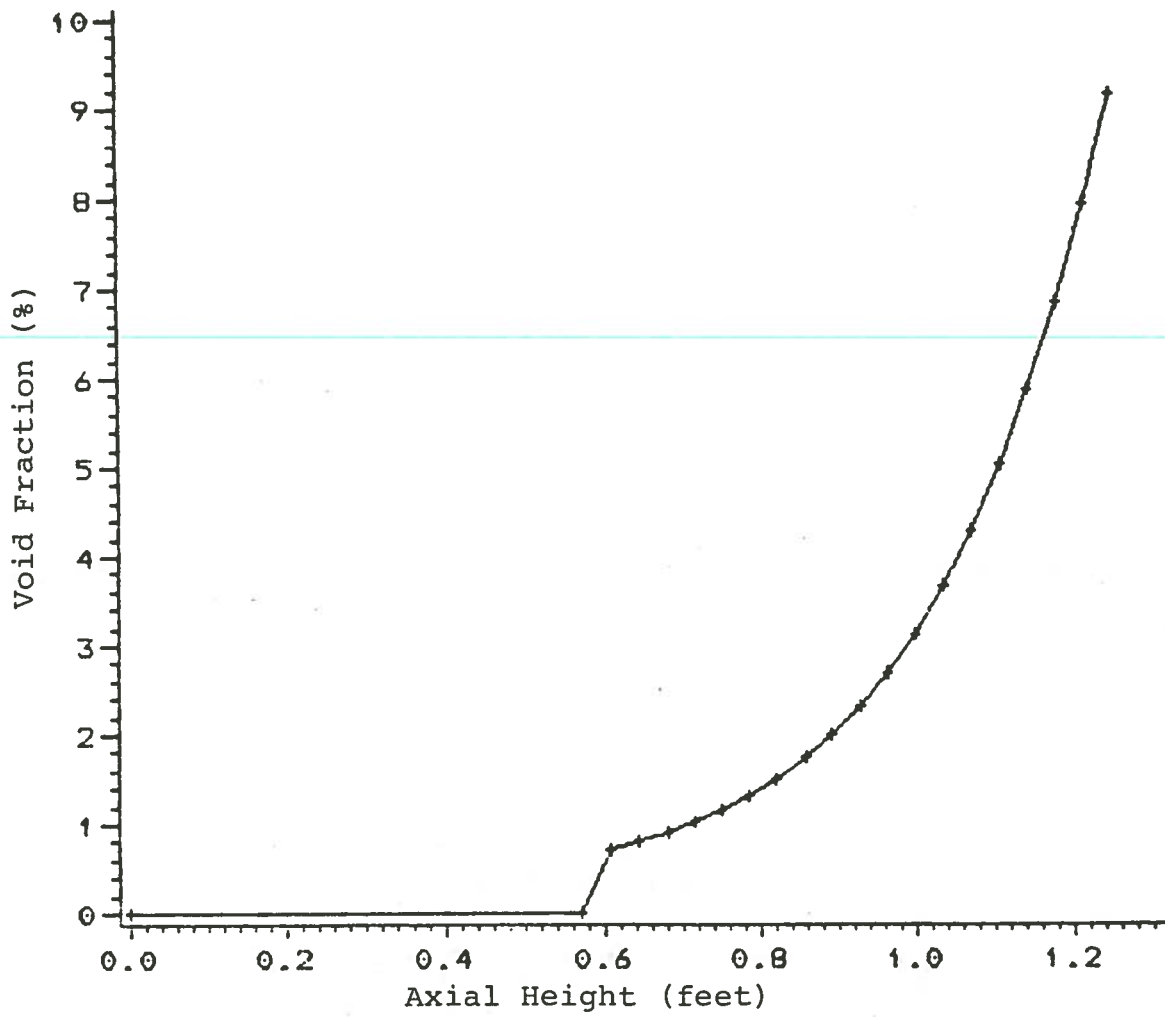
Figure 5-4

Void Fraction Profile

Table 5-7

Input for 1.0 MW Upgraded NRAD Case

| | |
|---|---|
| Inlet Pressure (psia) | 16.302 |
| Outlet Pressure (psia) | 15.086 |
| Inlet Temperature (°F) | 90 |
| Reactor Power (MW) | 1.0 |
| Channel Power (KW) | 17.338 |
| Axial Peaking Factor | 1.26 |
| Number of Axial Increments | 35 |
| Maximum Flow Rate Convergency Error ($lb_m$/hr) | 0.01 |
| Maximum Steam Quality Convergency Error (%) | 1.0 |

Table 5-8

NAFQ Results for 1.0 MW Upgraded NRAD Case

| | |
|---|---|
| Mass Flow Rate  ($lb_m/hr$) | 574 |
| Minimum Subcooling (°F) | 20.2 |
| Maximum Void Fraction (%) | 1.88 |
| Minimum DNBR | 3.62 |
| Maximum Cladding Temperature (°F) | 259 |

These results will be compared in the next section to
the results for the 1.2 MW PRNC case.

## 5.3. Comparison of 1.0 MW NRAD and 1.2 MW PRNC Results

The results from Section 5.2 for the 1.0 MW
NRAD core are compared in this section to the results
calculated by the NAFQ program for the PRNC core at a
power of 1.2 MW, the power at which the PRNC reactor
experienced power oscillations.  The input parameters
to the NAFQ program for the 1.2 MW PRNC calculation are
given in Table (5-9).  The only difference between this
input and the input for the 2.0 MW PRNC case, given in
Section 5.1.2, is the reactor power.

In Table (5-10), the NAFQ results for the 1.2 MW
PRNC case are compared to the NAFQ results from Section
5.2.1 for the 1.0 MW NRAD design case.  The maximum void
fraction in the NRAD case is more than six times as large
as in the PRNC case.  This is strong evidence that the
1.0 MW NRAD reactor with the present heat removal
system will suffer from power oscillations at a power
well below the design power of 1.0 MW.  The primary
reasons for this much larger void fraction are the
differences in inlet temperature, tank temperature, and
saturation temperature between the NRAD and PRNC
reactors.  The effects on the NAFQ results of variations
in these parameters will be shown in Section 5.4.

Table 5-9

Input For 1.2 MW PRNC Case

| | |
|---|---|
| Inlet Pressure (psia) | 25.157 |
| Outlet Pressure (psia) | 23.945 |
| Inlet Temperature (°F) | 90 |
| Reactor Power (MW) | 1.2 |
| Radial Peaking Factor | 1.54 |
| Axial Peaking Factor | 1.26 |
| Number of Fuel Elements | 95 |
| Number of Axial Increments | 35 |
| Maximum Flow Rate Convergency Error ($lb_m$/hr) | 0.01 |
| Maximum Steam Quality Convergency Error (%) | 1.0 |

Table 5-10

Comparison of 1.0 MW NRAD Case to 1.2 MW PRNC Case

|  | NRAD | PRNC |
|---|---|---|
| Reactor Power (MW) | 1.0 | 1.2 |
| Inlet Temperature (°F) | 120 | 90 |
| Mass Flow Rate ($lb_m$/hr) | 684 | 541 |
| Maximum Heat Flux (BTU/hr-ft$^2$) | $1.61 \times 10^5$ | $1.81 \times 10^5$ |
| Minimum Subcooling (°F) | 6.82 | 24.7 |
| Maximum Void Fraction (%) | 9.14 | 1.46 |
| Average Saturation Temperature (°F) | 215 | 239 |
| Minimum DNBR | 3.95 | 3.12 |

The results for the 1.0 MW NRAD reactor with
upgraded heat removal system are compared in Table
(5-11) to the results for the 1.2 MW PRNC case.  The
upgraded heat removal system results in a maximum void
fraction in the NRAD core about the same as that in the
1.2 MW PRNC core.  Therefore, with the tank and inlet
temperatures assumed for the upgraded heat removal system,
the 1.0 MW NRAD core is predicted to operate at the
threshold of power oscillations.

## 5.4.  Sensitivity Results

The sensitivity of the NAFQ program to selected
input errors is investigated in this section.  The
procedure used is to vary the input parameters one at a
time and compare the perturbed results for each input
variation with the results for an unperturbed case.
The case used as a base for this sensitivity study is
the 1.0 MW NRAD design case, presented in Section 5.2.1.

The input parameters changed and the calculated
results for each variation are given in Table (5-12).
These results are compared to the base, or unperturbed,
case in Table (5-13).  From the results in Table (5-13),
it can be seen immediately that the number of axial nodes
has very little effect on the calculated results, at
least in this range of nodalization.  The remaining
input variations represent the maximum expected

Table 5-11

Comparison of 1.0 MW Upgraded NRAD
Case to 1.2 MW PRNC Case

|  | NRAD | PRNC |
|---|---|---|
| Reactor Power (MW) | 1.0 | 1.2 |
| Inlet Temperature (°F) | 90 | 90 |
| Mass Flow Rate  ($lb_m$/hr) | 574 | 541 |
| Minimum Subcooling (°F) | 20.2 | 24.7 |
| Maximum Void Fraction (%) | 1.88 | 1.46 |
| Average Saturation Temperature (°F) | 215 | 239 |
| Minimum DNBR | 3.62 | 3.12 |

Table 5-12

Sensitivity Results

| Parameter Changed | Input Value | Flow Rate (lb$_m$/hr) | Minimum Subcooling (°F) | Maximum Void Fraction (%) | Minimum DNBR |
|---|---|---|---|---|---|
| Power | +20% | 818 | 4.48 | 15.4 | 3.52 |
| Loss Coefficients | +10% for all | 682 | 6.46 | 9.64 | 3.94 |
| Condensation Coefficients | +25% | 676 | 5.80 | 9.27 | 3.93 |
| Pressure | − 1 psia | 706 | 6.01 | 10.4 | 4.01 |
| Axial Peaking Factor | −10% | 685 | 6.89 | 10.3 | 3.95 |
| Inlet Temperature | +10°F | 766 | 6.00 | 10.8 | 4.18 |
| Tank Temperature | +20°F | 673 | 5.35 | 11.4 | 3.92 |
| Axial Nodes | 30 | 684 | 6.80 | 9.16 | 3.95 |
| Axial Nodes | 40 | 684 | 6.79 | 9.18 | 3.95 |
| Axial Nodes | 45 | 684 | 6.81 | 9.16 | 3.95 |

Table 5-13

Sensitivity Results in Percent Difference

| Parameter Changed | Input Value | Percent Differences* | | | |
|---|---|---|---|---|---|
| | | Flow Rate | Minimum Subcooling | Maximum Void Fraction | Minimum DNBR |
| Power | +20% | +20 | -34 | +68 | -11 |
| Loss Coefficients | +10% for all | -0.3 | -5 | +5 | -0.3 |
| Condensation Coefficient | +25% | -1 | -15 | +1 | -0.5 |
| Pressure | -1 psia | +3 | -12 | +14 | +2 |
| Axial Peaking Factor | -10% | +0.1 | +1 | +13 | 0 |
| Inlet Temperature | +10°F | +12 | -12 | +18 | +6 |
| Tank Temperature | +20°F | -2 | -22 | +25 | -0.8 |
| Axial Nodes | 30 | 0 | -0.4 | +0.2 | 0 |
| Axial Nodes | 40 | 0 | -0.4 | +0.4 | 0 |
| Axial Nodes | 45 | 0 | -0.1 | +0.2 | 0 |

* These percent differences are with respect to the 1.0 MW NRAD design case.

uncertainties for each input parameter.  It can be seen
that each of these input variations caused the subcooling
to decrease and the void fraction to increase.  Thus,
input errors of the same arithmetic sign as the input
variations in Table (5-13) are conservative.  These
results are consistent with the expected behavior of
the NAFQ program.

As mentioned in Section 5.3, changes in the
inlet temperature, tank temperature, and saturation
temperature strongly influence the calculated void
fraction.  In addition, changes in the reactor power have
a strong effect on the void fraction.  It should be
remembered that a 20% increase in the reactor power means
a greater increase in the hot channel power, because of
the power peaking in the core.

Overall, the NAFQ program is not overly sensitive
to input errors, with the exception that the maximum
void fraction is very sensitive to power.  None of the
sensitivities presented here are strong enough to change
the conclusions drawn in the previous sections.

## Chapter 6

### CONCLUSIONS AND RECOMMENDATIONS

Based on the results presented in Chapter 5, it is concluded that the NAFQ program predicts approximately the thermal-hydraulic conditions in low power nuclear reactor cores in natural circulation at near atmospheric pressures. Since the program results agree reasonably well with the FSAR results, and FSAR calculations are always conservative, the NAFQ program can be used for safety analysis calculations.

With respect to the 1.0 MW NRAD design, it is concluded that the NRAD reactor as currently designed will not be able to operate at 1.0 MW without serious power oscillations caused by relatively large void fractions in the high power channels. The maximum cladding temperature and minimum DNBR limits will not be violated in the 1.0 MW core. It is recommended that the currently proposed configuration for the 1.0 MW core be changed. The NAFQ program can be used in designing a NRAD reactor system which will be free of power oscillations.

Finally, more program verification is recommended. Several studies are needed: first, comparison of NAFQ results to results from other core

thermal-hydraulic computer programs; second, measurement of the maximum flow rate, channel exit temperature, and void fraction in the existing 0.3 MW NRAD core and comparison of these measurements to the NAFQ results for the 0.3 MW NRAD case given in Section 5.1.1; and third, comparison of the NAFQ void fraction calculation to experimental data at the flow rates, pressures, and heat fluxes present in the NRAD core.

# REFERENCES

1.  Private communication from Gordon West, General
    Atomic Co., San Diego, California, 1982.

2.  "HFEF/N Neutron Radiography Facility Reactor, Final
    Safety Analysis Report," Document Number W0170-
    0015-SA-00, Argonne National Laboratory-West,
    Idaho Falls, ID, 1977.

3.  "Technical Specifications for HFEF/N Neutron
    Radiography Reactor," Document Number W0170-
    0016-SA-02, Argonne National Laboratory-West,
    Idaho Falls, ID, 1981.

4.  "RETRAN-02-A Program for Transient Thermal-Hydraulic
    Analysis of Complex Fluid Flow Systems," EPRI
    NP-1850, Electric Power Research Institute,
    Palo Alto, CA, 1981.

5.  Tong, L. S., and Weisman, J., _Thermal Analysis of
    Pressurized Water Reactors_, First Edition,
    American Nuclear Society, La Grange Park, IL,
    1970.

6.  Mendler, O. J., A. S. Rathbun, N. E. Van Huff, and
    A. Weiss, "Natural Circulation Tests With Water
    at 800 to 2000 psia Under Non-Boiling, Local
    Boiling, and Bulk Boiling Conditions," _Trans.
    ASME, Series C, J. Heat Transfer_, Vol. 83, No.
    261, 1961.

7.  Rouhani, S. Z., and E. Axelsson, "Calculation of
    Void Volume Fraction in the Subcooled and Quality
    Boiling Regions," _Int. J. Heat Mass Transfer_,
    Vol. 13, pp. 383-393, 1970.

8.  Lahey, R. T., Jr., "Two-Phase Flow in Boiling Water
    Nuclear Reactors," NEDO-13388, General Electric
    Co., San Jose, CA, 1974.

9.  Saha, P., and N. Zuber, "Point of Net Vapor
    Generation and Vapor Void Fraction in Subcooled
    Boiling," _Proc. Fifth Int. Heat Transfer Conf._
    Vol. 4, Tokyo, Sept., 1974.

10. "Safeguards Summary Report for the Puerto Rico Nuclear Center," Unpublished Report, Contract No. AT-(40-1) 3856, Puerto Rico Nuclear Center, Magaguez, Puerto Rico, 1969.

11. Baroczy, C. J., "A Systematic Correlation for Two-Phase Pressure Drop," Chemical Engineering Symposium Series, Vol. 62, No. 64, 1966.

12. Ginoux, J. J., Two-Phase Flows and Heat Transfer With Application to Nuclear Reactor Design Problems, McGraw-Hill Publishing Co., New York, NY, 1978.

13. Collier, J. C., Convective Boiling and Condensation, Second Edition, McGraw-Hill Publishing Co., New York, NY, 1981.

14. Holman, J. P., Heat Transfer, Fifth Edition, McGraw-Hill Publishing Co., New York, NY, 1981.

15. Tong, L. S., Boiling Heat Transfer and Two-Phase Flow, John Wiley and Sons, New York, NY, 1965.

16. Halliday, D., and R. Resnick, Fundamentals of Physics, John Wiley and Sons, New York, NY, 1974.

17. Jordan, D. P., and G. Leppert, "Pressure Drop and Vapor Volume with Subcooled Nucleate Boiling," Int. J. Heat Mass Transfer, Vol. 5, pp. 751-761, 1962.

18. Private communication from Wade Richards, Argonne National Laboratory-West, Idaho Falls, Idaho, 1983.

# Appendix A

## NOMENCLATURE

| | |
|---|---|
| A | Factor in Equation (3-42) |
| A | Channel cross-sectional area, $ft^2$ |
| $A_f$ | Flow area in fuel element channel, $ft^2$ |
| $A_1$ | Flow area upstream of area change, $ft^2$ |
| $A_2$ | Flow area downstream of area change, $ft^2$ |
| $A_j$ | Smaller of areas $A_1$ and $A_2$, $ft^2$ |
| b | Exponent in Equation (3-26) |
| $C_p$ | Liquid specific heat, $BTU/lb_m$-°F |
| $C_o$ | Void concentration coefficient |
| D | Fuel element diameter, ft |
| $\Delta Q_b$ | Power into steam generation, BTU/hr |
| $\Delta Q_c$ | Power into steam condensation, BTU/hr |
| $\Delta p$ | Pressure drop, $lb_f/ft^2$ |
| $\Delta Z$ | Length of an axial increment, ft |
| $D_H$ | Hydraulic diameter, ft |
| DNBR | Departure from nucleate boiling ratio |
| $e_v$ | Irreversible pressure loss coefficient |
| f | Friction factor |
| $F_{XY}^Q$ | Radial peaking factor |
| $F_Z^Q$ | Axial peaking factor |
| g | Acceleration due to gravity, $4.17 \times 10^8$ $ft/hr^2$ |
| G | Mass flux, $lb_m/ft^2$-hr |

76

$g_c$      Gravitational conversion factor, $4.17 \times 10^8$ $\dfrac{\text{lbm-ft}}{\text{lb}_f\text{-hr}^2}$

Gr      Grashof number

$H_{core}$      Height of core flow channel, ft

$h_{fg}$      Latent heat, $\text{BTU/lb}_m$

$H_{SP}$      Heat transfer coefficient, $\text{BTU/ft}^2\text{-hr-}°F$

$H_o$      Condensation coefficient in Equation (3-22), $1/°F$

k      Thermal conductivity, $\text{BTU/ft-hr-}°F$

N      Number of axial increments

p      Absolute pressure, $\text{lb}_f/\text{ft}^2$

$P_H$      Flow channel heated perimeter, ft

q"      Heat flux, $\text{BTU/ft}^2\text{-hr}$

$Q_{channel}$      Thermal power in flow channel, BTU/hr

$Q_{element}$      Thermal power in fuel element, BTU/hr

Re      Reynold's number

RHF      Relative heat flux

T      Bulk liquid temperature, °F

$T_s$      Saturation temperature, °F

$T_w$      Wall (cladding) temperature, °F

V      Volume, $\text{ft}^3$

$V_{fg}$      Difference between liquid and vapor specific volumes, $\text{ft}^3/\text{lb}_m$

$V_{gj}$      Drift velocity, ft/hr

$V'$      Momentum specific volume, $\text{ft}^3/\text{lb}_m$

W      Mass flow rate, $\text{lb}_m/\text{hr}$

X      Steam quality

Z      Axial distance from beginning of heated length, ft

## Greek Letters

$\alpha$      Void fraction

$\beta$      Steam volumetric flow fraction

$\beta$      Thermal expansion coefficient, $1/°F$

$\mu$      Liquid viscosity, $lb_m/ft\text{-}hr$

$\Omega$      Mass flux correction factor

$\phi_{fo}^2$      Two-phase friction factor

$\phi_{fo}^{2\prime}$      Two-phase friction factor for $G = 10^6 \ lb_m/ft^2\text{-}hr$

$\rho$      Density, $lb_m/ft^3$

$\bar{\rho}$      Two-phase density, $lb_m/ft^3$

$\sigma$      Surface tension, $lb_f/ft$

$\theta$      Liquid subcooling, $°F$

## Subscripts

a      Acceleration

avg      Average

b      Bulk

cond      Condensation

crit      Critical

d      Void departure point

e      Elevation

f      Friction

f      Film

| | |
|---|---|
| g | Saturated vapor phase |
| i | Increment i |
| in | Inlet |
| iso | Isothermal |
| j | Area change number |
| k | Beginning of increment i |
| k+1 | End of increment i |
| $\ell$ | Local |
| $\ell$ | Liquid |
| LH | Heated length |
| LR | Lower reflector |
| max | Maximum |
| out | Outlet |
| SCB | Subcooled boiling |
| tot | Total |
| TP | Two-phase |
| UR | Upper reflector |

## Appendix B

## DERIVATION OF HEAT FLUX EQUATION

The heat flux equation given by Tong and Weisman is

$$q'' = q''_{mas} \cos \left(\frac{\pi Z'}{L_o}\right), \qquad \text{(B-1)}$$

in which $Z'$ is the axial distance from the center of the fuel element and $L_o$ is the extrapolated length of a half-cycle of the cosine curve.[5] This equation is transformed to a more useful form by making use of the ratio $L'/L_o$, where $L'$ is the difference between the actual heated length and the extrapolated length. These terms are shown in Figure (B-1).

Letting

$$A = \frac{L'}{L_o} \qquad \text{(B-2)}$$

gives

$$L' = A L_o. \qquad \text{(B-3)}$$

Since

$$L_H = L_o + L', \qquad \text{(B-4)}$$
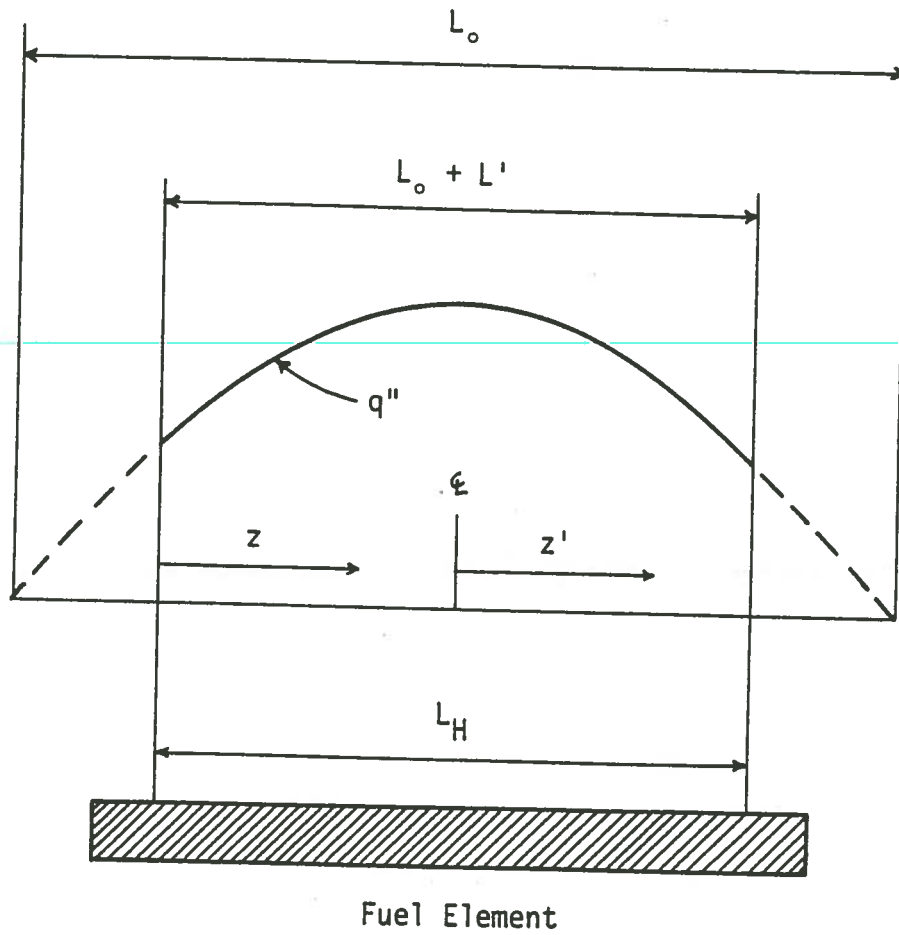
the variable $L'$ from Equation (B-3) is substituted into

Figure B-1

Axial Heat Flux Geometry

Equation (B-4) to yield

$$L_H = L_o + AL_o, \tag{B-5}$$

or

$$L_o = \frac{L_H}{1+A} . \tag{B-6}$$

By definition:

$$F_Z^Q = \frac{q''_{max}}{q''_{avg}} , \tag{B-7}$$

or equivalently:

$$q''_{max} = F_Z^Q \, q''_{avg}. \tag{B-8}$$

Substituting Equations (B-6) and (B-8) into Equation (B-1) gives

$$q'' = F_Z^Q \, q''_{avg} \, \cos \left[\frac{\pi (1+A) Z'}{L_H}\right]. \tag{B-9}$$

The variable $Z'$ is defined as

$$Z' = Z - \frac{L_H}{2} , \tag{B-10}$$

in which Z is the axial distance from the beginning of the heated length. By substituting Equation (B-10) into Equation (B-9), the equation given in Chapter 3 for

calculating the local heat flux results:

$$q'' = F_Z^Q q'' \cos \left[ \frac{\pi (1+A) (Z - L_H/2)}{L_H} \right].$$ (B-11)

The ratio A is calculated from the equation:[5]

$$F_Z^Q = \frac{\pi (1+A)}{2 \sin \left[ \frac{\pi}{2} (1+A) \right]}$$ (B-12)

by solving for A.

# Appendix C

## DETERMINATION OF CONDENSATION COEFFICIENT

The value of the condensation coefficient in the void fraction calculation, $H_o$ in Equation (3-20), was determined from the experimental data of Jordan and Leppert.[17] This data is generally not useful for practical void fraction calculations; instead, it is used to find an approximate value of the condensation coefficient. The data used is for a heat flux of $5 \times 10^5$ BTU/ft$^2$-hr, a flow velocity of 4 ft/sec, a pressure of from 15 to 21 psia, and a bulk liquid temperature ranging from 86°F to 121°F. For these conditions, the void fraction is a nearly constant 0.69% over the heated length. The geometry and thermal-hydraulic conditions from this data were input to the NAFQ program and the condensation coefficient was varied until the maximum calculated void fraction was slightly less than that given by the Jordan and Leppert data. The value of the coefficient determined in this manner was 8700 1/°F, for a void fraction which varies from 0.32% to 0.67%. Since the condensation coefficient is over-estimated for this data, the void fraction calculated by the NAFQ program should be conservative.

## VITA

Howard Brodt was born in Jacksonville, Florida, on August 24, 1956. He graduated from Mid-City Baptist High School in 1974, and from Louisiana State University in 1980 with a Bachelor's degree in Landscape Architecture. He is presently working for Middle South Services in the area of thermal-hydraulic transient analysis and is a candidate for the degree of Master of Science in Nuclear Engineering.